Folding Photopolymerized Origami Sheets by Post-Curing

Xiaodong HE

A Thesis

in

The Department

of

Mechanical, Industrial

and

Aerospace Engineering

Presented in Partial Fulfillment of the Requirements

for the Degree of Master of Sciences (Mechanical Engineering) at

Concordia University

Montreal, Quebec, Canada

May 2020

CONCORDIA UNIVERSITY
School of Graduate Studies

This is to certify that the thesis prepared

By: Xiaodong HE

Entitled: Folding Photopolymerized Origami Sheets by Post-Curing

and submitted in partial fulfillment of the requirements for the degree of

Master of Applied Science

complies with the regulations of the University and meets the accepted standards with respect to originality and quality.

Signed by the final examining committee:

Dr. Rolf Wuthrich — Chair

Dr. Rolf Wuthrich — Examiner

Dr. Martin Pugh — Examiner

Dr. Tsz Ho Kwok — Thesis Supervisor(s)

Approved by Waizuddin Ahmed — Chair of Department or Graduate Program Director

MOURAD DEBBABI Dean,

Date

Abstract

Folding Photopolymerized Origami Sheets by Post-Curing

by Xiaodong HE

Origami,which is generally fabricated from one single sheet of paper by sequential folding, has enjoyed a high popularity during the past centuries. Because of the deployability and ability to reconfigure its shape, it is a promising structural design technique that is utilized in biomedical and aerospace engineering. The purpose of this paper is to present a novel manufacturing approach to fabricate origami based on 3D printing utilizing digital light processing. Specifically, it is proposed to leave part of the model uncured during the printing step, and then cure it in the post-processing shape-setting step in the folded configuration. While the cured regions in the first step try to regain their unfolded shape, the regions cured in the second step try to keep their folded shape. As a result, the final shape will be obtained when both regions stresses reach equilibrium. Finite element Analysis is performed in ANSYS to obtain the stress distribution on common hinge designs. This proves that the square-hinge has a lower maximum principal stress compared with elliptical and triangle hinges. Based on the square-hinge and rectangular cavity two variables, the width of the hinge and height of the cavity, are selected as principal variables to construct relationships between the two parameters and final folding angle. In the end, experimental verification show that the developed method is valid and reliable to realize the proposed deformation and 3D development of 2D hinges.

Contents

List of Figures

List of Tables

Chapter 1

Introduction

Origami, stemming from the ancient Japanese art, has gained popularity in the past centuries because of its ability to create complex three-dimensional (3D) shapes from a two-dimensional (2D) sheet of paper strictly by using folding techniques. Due to its attractive feature simply requiring a 2D manufacturing process, origami has been applied in many engineering applications to build up 3D shapes [1], such as protective articles [2], aerospace [3], communication equipment [4] and medical device [5]. In these cases, engineering materials with non-negligible thickness are applied so that the part can have necessary stiffness to perform different functions. However, to fold the materials with non-negligible thickness and hold the final shape, certain assembly steps or mechanical fasteners are needed, otherwise it is limited to the materials that can have plastic deformation (e.g., ductile metal and paper through delamination of layers). Recently, there are various self-folding mechanisms proposed for the fabrication of origami-based products. For example, smart materials like shape-memory polymers or alloys are applied to deform shapes in a pre-programmed manner [6]. Additionally, concepts such as four-dimensional (4D) printing, achieved through selective material placement during 3D printing [7], allows for new self-folding mechanism through non-homogeneous deformation by combining materials with different expansion ratios [8]. The self-folding mechanisms require the use of either smart materials or multiple materials. However, the limited choices of smart materials and the complexity of multi-material fabrication hinder a wider use of origami structures in engineering applications. Although there are some works [9] utilizing a single material by precisely controlling the manufacturing process to create anisotropic deformations, the range of manufacture thickness was highly constrained.

1.1 Motivation

Based on the above challenge, the motivation is *how to expend the use of 'non-smart' materials in origami, such that they can be fabricated in 2D and folded to their final 3D shapes?* This motivates the research to develop a user-friendly way to apply non-smart materials to origami-based products, without increasing the complexity of the manufacturing process. Since the manufactured part needs to be deformed to its final shape, this thesis primarily focuses on elastic materials.

1.2 Novelty and Contribution

To address the research question, this thesis revisited the 3D printing technologies to search for possibilities. It is observed that many 3D printing processes need a post-processing step. For example, the fused deposition method (FDM) applies vaporization [10] or coating [11] after printing to improve the surface finishing; the selective laser sintering (SLS) method applies a post-sintering step to increase density and enhance the mechanical strength of the printed parts [12]; the stereolithography (SLA) or digital light processing (DLP) technology has a post-curing step to maximize the material's physical properties.

With this observation, it is hypothesized that deforming a 3D-printed part in the post-processing step will enable it to keep the final deformed shape, even after all external stimulus are removed. If it is tested true, it will be able to make use of the post-processing step to realize the folding to final shapes for non-smart materials. To test this hypothesis and study the extent of its ability to keep the deformed shape, this thesis pick the DLP 3D printing technology for a proof-of-concept, study the principle of its post-curing operation, and develop the design and manufacturing methodology to allow shape-retention. DLP 3D printing takes advantage of digital light projector to cure a photopolymer resin layer-by-layer, and the post-curing is similar to a second solidification step after the initial 3D printing. The goal is to make use of this two-step curing process to introduce different stresses within the model such that it will retain its 3D shape. Specifically, it is proposed to leave part of the model uncured during the printing step, and then cure it in the post-processing curing step after folding. In this way, while the regions cured in the first step tend to go back to the unfolded shape, the

regions cured in the second step try to keep its folded shape. As a result, the final shape will be obtained by the balance between them, i.e., at equilibrium of the stresses.

The contributions of the thesis comes from developing and testing such a methodology, which are summarized as follows.

- A new approach is developed to fabricate 3D shapes from 2D geometry, requiring no assembly, and without changing the DLP 3D printing manufacturing pipeline.
- Various geometries are studied, and a new hinge design is developed to trap the uncured material during 3D printing and allow folding without leaking the material.
- To maximize the extent of plastic deformation and allow the control of it, a mathematical relationship between the folding angle and the hinge geometry is obtained experimentally.

Several origami examples are also fabricated to demonstrate the capability of the proposed method, and the experimental results verify that the parts fabricated by 2D elastic material can hold the shapes in 3D and possess the origami characteristics.

1.3 Thesis Outline

The rest of this thesis is organized as follows. In Sec. 2, a brief overview of current research is presented. The technological background and experimental setup, as well as the material characterization, are introduced in Sec. 3. In Sec. 4, the framework of the methodology is stated in details, including the design of hinge and the mathematical model of folding angle. In Sec. 5, some testing cases with a few demonstrated uses of the method are presented, and the thesis is concluded in Sec. 6.

Chapter 2

Literature Review

This paper is related to origami fabrication, 3D printing and SLA/DLP with post-curing, the related works are present below respectively.

2.1 Origami modeling

Origami is a compound word connecting ori- and -kami together, which separately mean fold and paper. A few scholars show enormous interest upon paper origami. Bowen et al. [13] described that an origami vertex, the point at which folded converge, was shown to be equivalent to a spherical change-point mechanism. The position analysis of an origami vertex was presented, resulting in a relationship between input and output angles as well as the path of the coupler link. Sareh and Guest [14] introduced the family of isomorphically generalized symmetric variations of the Miura-ori, they studied the Miura crease pattern as a wallpaper pattern and reduced the symmetry of the original crease pattern to design new patterns while at the same time preserving the symmetry group of the tessellation as well as the flat-foldability condition at each node. Fuchi et al. [15] investigated strategies for design optimization to incorporate the current and future configurations of the structure in the performance evaluation. An optimization method combined with finite-element analysis was used to distribute mechanical properties. Dudte et al. [16] showed that scale-independent elementary geometric constructions and constrained optimization algorithms could be utilized to determine spatially modulated patterns that yielded approximations to given surfaces of constant or varying curvature.

In modeling, from an origami fold, in the research of Jacobsen et al. [17], lamina emergent mechanisms (LEM)was defined, and framework was proposed on which to base future

LEM design, which includes the fundamental components created by influencing geometry, material properties, and boundary conditions and basic mechanisms. Wilding et al. [18] combined the unique motion of spherical mechanisms with the compactness and simple topology of LEMs. In the paper, it is stated that 21 of the 33 possible spherical 4R types can be spherical LEMs, and the classification was used to predict motion capabilities of spherical 6R mechanisms. Wonoto et al. [19] presented a research study on a geometry and mechanism of origami for generating a deployable tessellation structure. By using geometric scripting with a parametric system and finite element analysis tools, the paper explored a combination of methods for understanding the structural limitations of deployable origami geometry. Saito et al. [20] expanded origami into designing morphing structures, and proposed a model to evaluate elastic deformation in nonrigid origami structures. The model was applied to deployable plate models. Sarah-marie belcastro et al. [21]modeled the folding of ordinary paper via piecewise isometrics R2 to R3. In the research, the necessity conditions from the more restrictive case of folding paper flat were generalized. And it was also proved that if the crease pattern is foldable, then the product of the associated rotational matrices was the identity matrix. In the work of Buskohl et al. [22] developed a design tool to identify optimal fold patterns for geometric and functional objectives based on topology optimization using mechanical analysis to distribute fold line properties within a reference crease pattern to achieve a target actuation. The fold stiffness optimization was then followed by a node position optimization, which determined that only two of the predicted topology were fundamental and the solutions from higher density grids were variants or networks of these building blocks.

Speaking of origami, the folding mechanism has to be mentioned, because it is essential part in realization of origami. Lobontiu et al. [23] developed closed-form compliance equations for conic-section (circular, elliptic, parabolic and hyperbolic) flexure hinges, finite element simulation results were used to confirm the theoretical formulation data. Yi et al. [24] designed a planar three degree-of-freedom (DOF) parallel-type micropositioning mechanism designed with the intention of accurate flexure hinge modeling. And a preliminary kinematic analysis that includes inverse kinematics, internal kinematics, and analytic stiffness modeling referenced to the task coordinate were presented. Tian et al. [25] presented the closed-form compliance equations for the filleted V-shaped flexure hinges. The in-plane and out-of-plane compliance of the flexure hinges were developed based on the Castigliano's

second theorem and also investigated the influences of the geometric parameters on the characteristics of the flexure hinges. Kang et al. [26] presented an analytic model of cartwheel flexure. 6-DOF (degrees of freedom) stiffness equations for cartwheel flexure were derived and verified by comparing the model's predictions with FEM (finite element method) simulations and experiments. Qiang et al. [27] presented a power-function-shaped flexure hinge. Based on the unit-load method, the closed-form compliance equations of the flexure hinge were derived. Additionally, the results were verified through finite element analysis. Qin et al. [28] established the linear and angular compliance models for a class of statically indeterminate symmetric (SIS) flexure structures. Computational analysis were performed to investigate the influence of the axial tension. Lobontiu et al. [29] put forward a general analytical model of the planar compliance for two-segment circular-axis symmetric notch flexure hinges. The model covered both relatively large radius-to-thickness ratio designs (thin flexures) and small radius-to-thickness ratio configurations (thick flexures). And the analytical compliance model for this flexure were confirmed by finite element analysis and experimental testing. Lobontiu et al. [30] proposed model the direct and inverse quasi-static response of constrained/over-constrained planar serial mechanisms with flexure hinges under folding, axial, and shear planar (three dimensional) loading and small deformations. The method used a basic three-point compliance matrix corresponding to one rigid link and one adjacent flexure hinge that are subjected to one-point load. In the study of Friedrich et al. [31], a nonlinear higher order finite beam element-based modeling approach was presented strongly reducing the computation time of nonlinear models. Using the method, Planar deformation and mechanical stress of a single circular flexure hinge under a wide range of loads were modeled and computed. Wang et al. [32] derived rotational compliance of cracked right circular flexure hinge by the superposition of the rotational compliance of flexure hinge and the compliance change induced by the crack. Noveanu et al. [33] proposed an analytical compliance-based matrix method to model the quasi-static, small-displacement response of planar branched flexure-hinge over-constrained mechanisms. The architectures was substructured or decomposed into simpler chains whose compliance were evaluated from known individual segment compliance. The substructured-chain compliance were subsequently combined with external loads to solve for unknown displacements and reactions and to further evaluate parameters relevant to the mechanism behavior. Parvari Rad et al. [34] investigated the spherical flexure based on spherical compliant mechanism. In the paper, each element

of the spherical flexure spatial compliance matrix is computed analytically as a function of both flexure dimensions and employed material. Yang et al. [35] designed a kind of planar symmetric superelastic flexure hinge. it was modeled by beam elements which consider the variation of the beam cross-section, and the geometric and material nonlinearities. Based on the model, the static responses of the planar symmetric superelastic flexure hinges with different notches are compared and analyzed. Liu et al. [36] presented a kind of multi-notched flexure hinge based on topology optimization, which consists of two right circular and two parabolic notches, for positioning stages based on compliant mechanisms. Besides, the paper also showed the stiffness, rotational precision and stress levels of the flexure hinges were developed using finite element analysis (FEA). Lai et al. [37] proposed mechanism consists of two L-shape lever-type mechanism and one bridge-type mechanism used on effective actuation stroke of piezoelectric actuator. Based on the stiffness matrix method, an analytical model was performed under certain constraints.

Cao et al. [38] presented a mixed mesh of flexure hinges and beams was employed to discretize the design domain, and their connectivity, locations, and sizes were simultaneously determined to fulfill both the stiffness-flexibility criterion (for efficiency) and a newly proposed input stroke criterion. Linß et al. [39] investigated the elasto-kinematic hinge and mechanism properties in dependence of scaling the geometric parameters regarding the impact of using optimized flexure hinge contours within a unified synthesis method without the need of rerunning simulations. Wu et al. [40] raised an analytical compliance matrix model of a flexure hinge and the conical-shaped notch flexure hinge was innovatively parameterized using the non-uniform rational B-spline (NURBS) curve, which was used to describe several different conical notch shapes, including the ellipse, parabola, and hyperbola. Chen et al. [41] developed a damped circular hinge with integrated comb-like substructures and derived a mathematical model of loss factor of the flexure hinge and built its pseudo-rigid body model with damping. Meanwhile, loss factor of the damped flexure hinge and its mathematical model were verified based on finite element analysis.

2.2 Origami fabrication

In fabrication, Christina L. Randall et al. [42] described the fabrication and in vitro characterization of lithographically structured and self-folded containers for immunoprotected cell

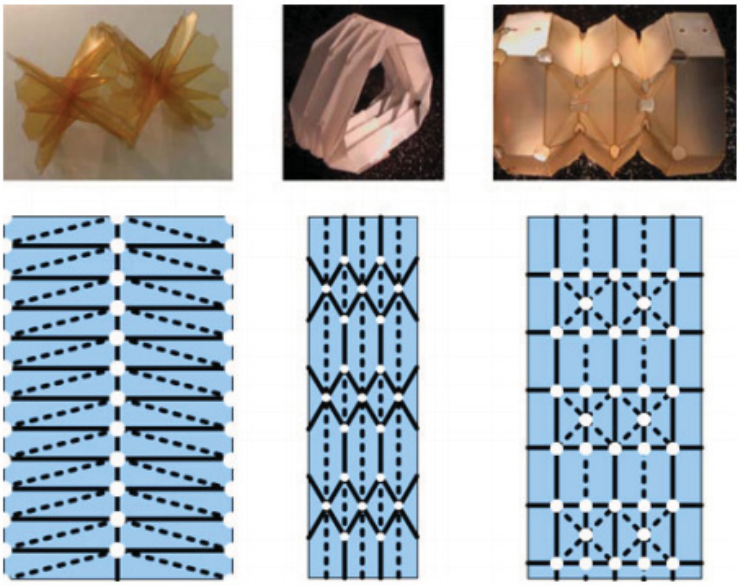

FIGURE 2.1: Three contractile segment designs we investigated for an origami-inspired worm robot (top), with their respective crease patterns (bottom): the diagonal pattern (left), the Yoshimura pattern (middle), and the waterbomb base pattern (right).© 2013 IEEE.

encapsulation. And their group fabricated containers with varying pore sizes and observed that pores sizes of approximately 78 nm were sufficient to significantly inhibit diffusion of IgG (the smallest antibody) and permit adequate diffusion of insulin. Edmondson et al. [43] designed a oriceps based on the spherical kinematic configurations of several origami models and can be fabricated by cutting and folding flat material, which had a potential in surgery. Onal et al. [44] employed laser-machined origami patterns to build a new class of robotic systems for mobility and manipulation, as shown in Fig. 2.1. For actuation, they used compact NiTi coil actuators embedded on the body to move parts of the structure on-demand. Miyashita et al. [45] presented a methodology and validation of print-and-self-fold electric devices, as seen in Fig. 2.2. By exploiting the unique material properties of MPF, they developed fundamental electric devices, namely a resistor, capacitor, and Felton et al. [46] developed a crawling robot that could fold itself. The robot started from a flat sheet with embedded electronics and transforms autonomously into a functional machine. The material used was shape-memory composites developed by themselves. Malacowski et al. [47] described the fabrication of arrayed or untethered single cell grippers composed of biocompatible and bioresorbable silicon monoxide and silicon dioxide. The energy required to actuate these grippers was derived from the release of residual stress. A finite element model was applied to predict these folding angles. Miyashita et al. [48] presented a sheet that can self-fold into a

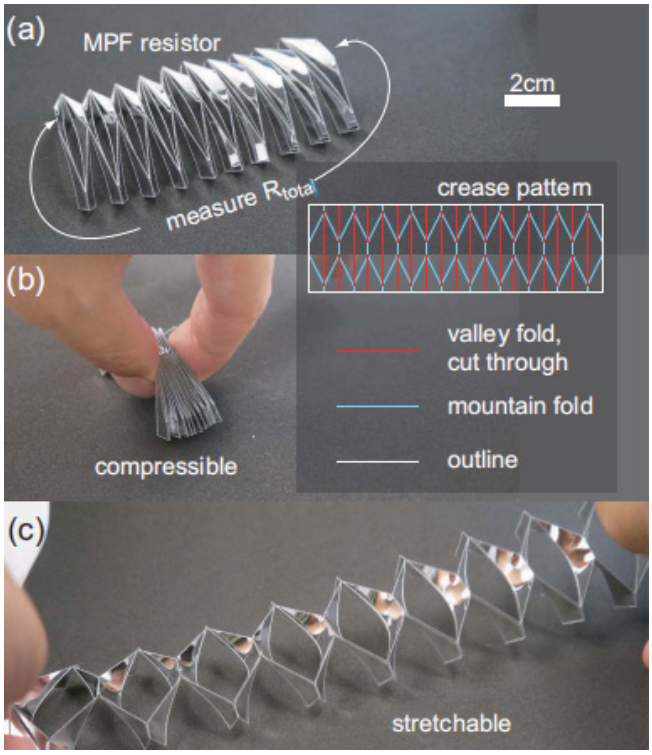

FIGURE 2.2: Designed MPF resistor at normal length (a), compressed (b), and stretched (c). © 2014 IEEE.

functional 3D robot,actuate immediately for untethered walking and swimming, which could be seen in Fig. 2.3. The robot was capable of conducting basic tasks and behaviors, including swimming, delivering/carrying blocks, climbing a slope, and digging. Sung et al. [49] showed how the basic joints used in robots can be constructed using print-and-fold. The patterns were parameterized so that users not only could the desired degrees of freedom but can also specify the joint's range of motion. The joints can be combined with each other to achieve higher degrees of freedom. Bowen et al. [50] developed a dynamic model to simulate the effect of active materials on an origami-inspired design, as seen in Fig. 2.4. The dynamic model of the origami waterbomb base, a well-known and foundational origami mechanism was developed using commercial software ADAMS 2014. Wheeler et al. [51] presented a quantitative metric—the origami compliance metric (OCM)—that aids in identifying proper modeling of a homogeneous origami structure based upon the compliance regime it falls into soft, hybrid, or mechanism-reliant, and detailed a theory of proper constraint by which an ideal soft structure's number of degrees-of-freedom may be approximated as 3n. Fang et al. [52] investigated the multi-stability characteristics of a stacked origami cellular solid consisting of multiple Miura-ori sheets, specifically focusing on a dual-cell chain structure. A

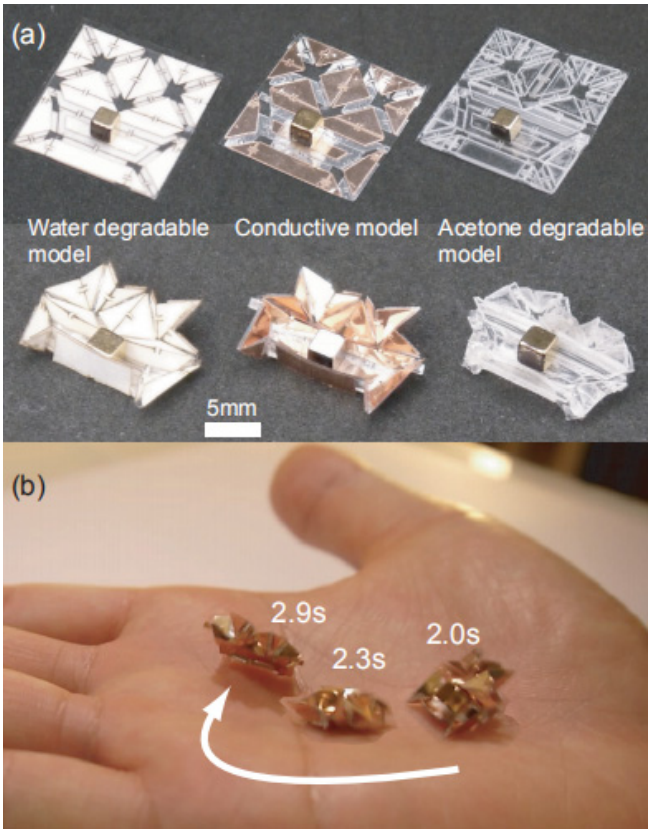

FIGURE 2.3: The developed origami robot. a) (From left to right) water-degradable model whose outer layer dissolves in water; conductive model (aluminum coated polyester); acetone-degradable model whose entire body (except magnet) dissolves in acetone. b) Self-folded robot (controlled by a magnetic field) walking on a palm. © 2015 IEEE.

geometric mechanics model was formulated to examine the underlying physical principles of the observed asymmetric behaviors.

2.3 3D printing origami

Fabricating origami is known to be complex, and there are some efforts trying to using 3D printing to manufacture origami products. Ge et al. [6] printed active composite by the PolyJet technology, in which shape memory fibers were embedded in an elastomeric matrix at the hinges to enable origami folding. Zhang et al. [53] printed black ink lines by a LaserJet printer as hinge patterns to control the folding angle and showed some examples based on finite element method. Ahn et al. [54] used diverse materials and combined direct-write and wet folding techniques to manufacture origami, with shapes ranging from simple polyhedra to intricate origami forms. Kimionis et al. [55] printed origami package with inkjet and DLP combination for high frequency application shown in Fig. 2.5. Wu et al. [56] presented

FIGURE 2.4: Polypropylene waterbomb samples were created with a laser cutter. Gray hatching indicates the ground panel. Permanent magnets with magnetization direction marked with black arrows were attached to each ungrounded panel to match the configuration determined from the dynamic model.

an approach to print reconfigurable antennas by combining Liquid Metal Alloy (LMA) microfluidics and Voronoi origami structures seen in Fig. 2.6. Mao et al. [57] printed sequential self-folding structures by thermal activation of spatially-variable patterns with digital shape memory polymers. However, all these methods either require the use of smart materials or an accurate external actuation is needed to fold the material. Liu et al. [58] fabricated the structure via 3D printing, the twisted tower was reconstructed in a computer aided design (CAD) model. The CAD model was then 3D printed using two different materials, and one was flexible material for creases and a rigid material for surfaces shown in Fig. 2.7. Klein et al. [59] constructed thin gel sheet which undergo laterally nonuniform shrinkage to bring the prescribed non-Euclidean metrics on the sheets come true, and he as well showed how buckling and wrinkling appeared on the sheet, offered guidelines on how to generate different features. Edmondson et al. [43] designed the Oriceps based on the spherical kinematic configurations and could be fabricated by cutting and folding. Because of its easy cleaning, quick wearing, small scale, great tool flexibility, it has a huge potential in medical industry. Qi Ge. et al. [60] took active composite embedded with shape memory fibers precisely printed in an elastomeric matrix as hinges to enable origami folding and also developed the theoretical model to guide the design parameters. In order to address non-flattenable structure problem, Kwok et al. [61] presented a shape optimization frame-work to improve non-flattenability by adding interior/boundary cuts, besides, also minimized the total length of inserted cuts

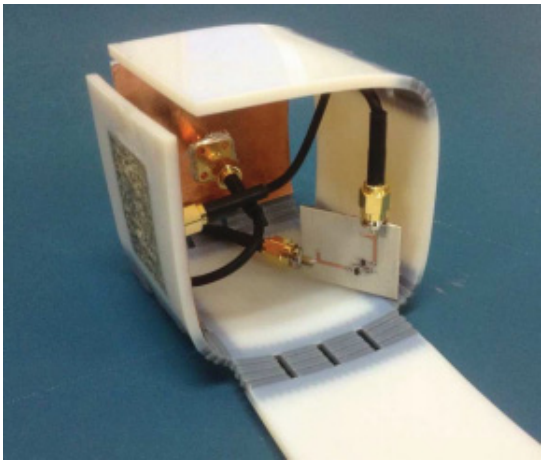

FIGURE 2.5: Origami package with harvester electronics inside. © 2015 IEEE.

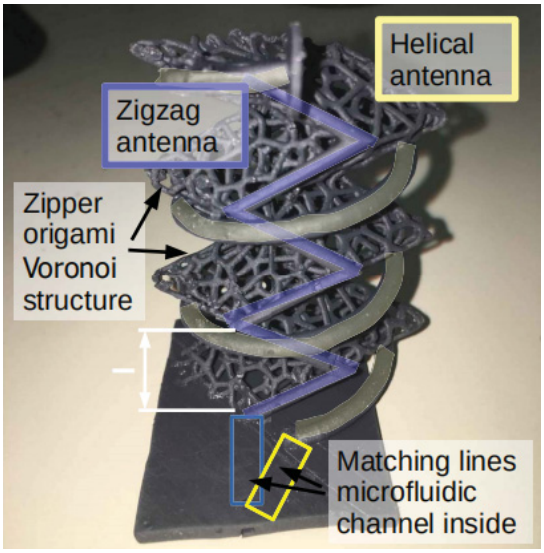

FIGURE 2.6: A photo of the 3D Printed origami antenna tree. The zigzag antenna and its matching circuit are marked in blue while helical antenna and its matching circuit in yellow. © 2018 IEEE.

to reduce artifacts. Mu et al. [62] put forward a laminated structure fabricated by bonding a stretched elastomer sheet between light activated polymers to provide a pre-programmed stress field. Once released, the elastomer could cause contraction and compression in light activated polymer, which are relaxed optically to trigger the desired deformation. He also developed a theoretical model to optimize the laminate design. Deng. et al. [63] showed a new self-folding and fabrication method without folding hinge, which could reconfigurate from 2D to 3D. The method used the different shrinkage property of different materials, and once heated up, the structure would deform over time to a 3D surface. Zhang et al. [64]

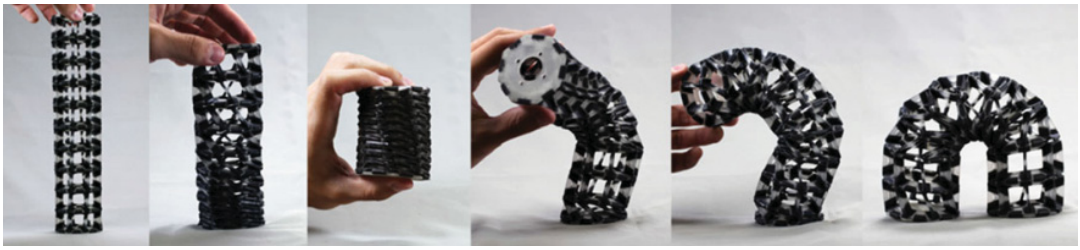

FIGURE 2.7: 3D printed origami tower consisting of 10 layers shown in different configurations. © 2018 IEEE.

used the width of ink line to control the folding angle, and also established a simplified localized bilayer folding model and corresponding finite element method to predict the final configuration.

2.4 SLA/DLP with post-curing

Post-curing is common method to enhance the properties in DLP printing. To be detailed, Kretzschmar et al. [65] compared the properties of parts fabricated by post-curing with concurrent curing and post-curing without concurrent curing. Salmoria et al. [66] correlated with mechanical properties after exposure of samples to ultraviolet radiation or thermal treatment, presenting layer sequence in the microstructure. Kuang et al. [67] presented a kind of ink containing photocurable resin and thermally curable epoxy resin for the digital light processing (DLP) 3D printing, and the material was cured twice, which were UV curing and elevated temperature sequentially, to increase the mechanical properties. Mitteramskogler et al. [68] used different light curing strategies and depths of cure for the 3D-printing of ceramic green parts and evaluated the influence of post-curing on cracks in the final ceramic. Kim et al. [69] tried to control and optimize dimensional accuracy, surface roughness, building orientation and mechanical properties of printed structures based on the glass transition temperature of the resin system under UV-curing. Steyrer et al. [70] studied the influence of photoinitiator selection and post-processing on the thermomechanical properties of various tough photopolymers. Wu et al. [71] studied the influence of post-curing on shape integrity and dimension accuracy and characterize the evolution of mechanical behavior of samples during post curing.

Chapter 3

Technological Background and Material

In terms of folding technology, a good deal of them were realized by the inhomogeneous expansion or contraction between layers or different materials. However, the fabrication of these methods is time-consuming and whole procedure is complex [7, 72, 73]. Furthermore, if the material is the same, structural thickness was seriously constrained [9]. In the method proposed, only one material is used to realize the transformation from $2D$ patch to $3D$ surface.

3.1 Digital Light Processing 3D Printing

Digital light processing (DLP) is a type of vat polymerization, which utilizes a photopolymer resin and a digital light projector as the light source to produce parts. A photopolymer is a photo-reactive polymer that is cured (or solidified) when exposed to light. Therefore, by sequentially projecting different mask images (black and white) layer-by-layer, different cross-sectional areas are fabricated, and a true 3D part is produced.

A typical processing sequence to fabricate a discrete part consists of shaping processes, property-enhancing operations, and finishing operations [74]. Similarly, the layer-by-layer projection is the shaping process in the DLP 3D printing, and it is followed by a post-curing process for enhancing the property of the part. During the shaping process, the exposure time for each layer is calibrated and optimized such that there is no under-curing or over-curing to maintain dimensional accuracy. However, the material is not completely cured during the shaping process. Therefore, after the whole part is shaped, it is soaked in an ultrasonic cleaner with 99% isopropyl alcohol for three minutes to wash away the residual resin on the surface,

TABLE 3.1: The material properties of the photo-polymer used in this study

Material parameter	*Value*
Density	$1100(kg/m^3)$
Viscosity at 77°F/25°C	1300-1500(cP)
Hardness(Shore)	82-85(A)
Ultimate strength	0.84(MPa)
Elongation at break	140(%)

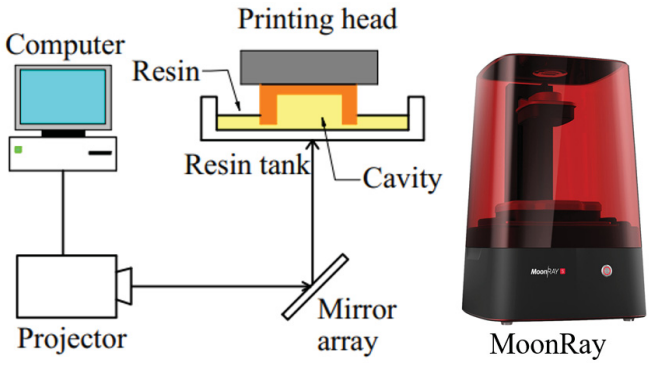

FIGURE 3.1: The mechanism of the DLP printing process and the MoonRay printer

and then it undergoes the post-curing step for ten minutes to reach its highest strength and stability. The post-curing step is often necessary and is especially important for functional resin [65, 71].

3.2 Experimental Setup and Material

In this paper, the MoonRay S100 DLP 3D printer produced by SprintRay is utilized. It uses the bottom-up approach, as illustrated in Fig. 3.1. The printing volume of the machine is $130mm \times 80mm \times 200mm$. The ultrasonic cleaner SS65 produced by Crystal Electronics, Inc. (Newmarket, ON) is used to remove the residual resin on the shaped part, and the LC-3DPrint Box produced by 3D Systems, Inc. (Rock Hill, SC) is employed for post-curing the material.

Deposit Light Process (DLP) is a sort of 3D printing technology, in which polymer is used to create models, prototypes, patterns, and production parts layer by layer, and during

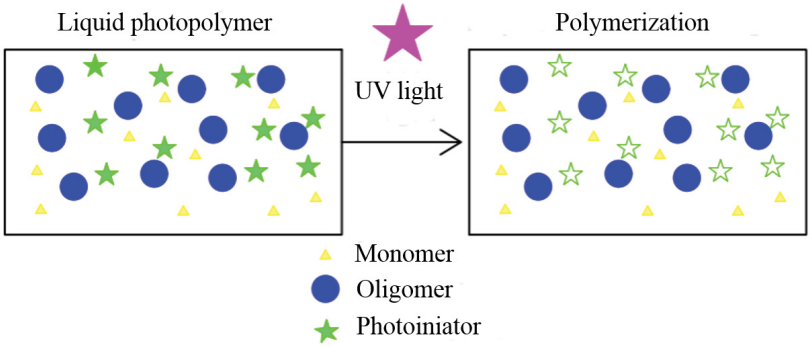

FIGURE 3.2: the mechanism of curing

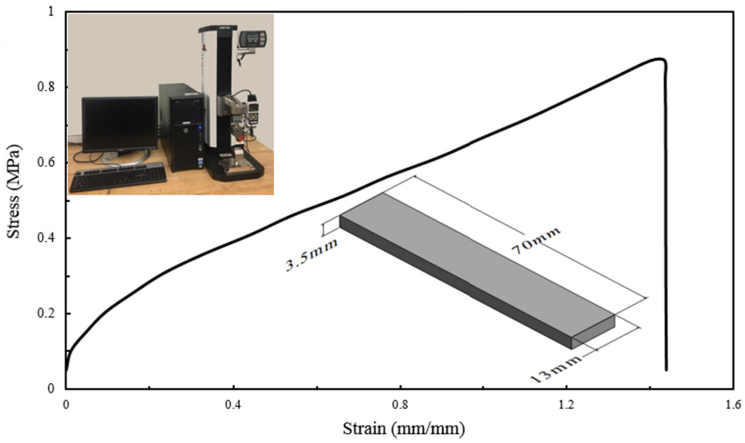

FIGURE 3.3: Stress-stain curve of the material used and experiment setting

that process photo-chemical action is performed to link chemical monomers together.

Typically a photo polymer consists of a mixture of monomers and oligomers in order to achieve the desired physical properties.Photopolymers undergo a process called curing. when curing, oligomers are cross-linked upon exposure to some certain kind of light. The result of photo curing is thermoset polymers.

Regarding the material used in this thesis, the material is a compound of monomer, oligomer and photoninitiator.Once exposed to UV light,the photoinitiator will be decomposed into reactive species, and the reactive species would initiate polymerization of specific functional groups on the oligomers. The mechanism could be seen in Fig. 3.2.

The resin used is the PT-F001MT Prototype Flex photopolymer produced by ApplyLab-Work (Torrance, CA), with its property presented in Table 3.1.

I am using a different manufacturing method than the producer's to fabricate the material as such, the mechanical properties of the material are obtained by a tensile test in this paper. Following the ASTM Standard Test Method D368, rectangular samples with the sizes of

$70mm \times 13mm \times 3.5mm$ are fabricated with the DLP 3D printer.

The testing is repeated ten times on the ESM750S motorized test stand, which is produced by Mark-10 Corporation (Copiague, NY). To ensure reliability and reproducibility of our method, the group with the lowest stress and strain is retained and shown in Fig. 3.3. From the graph, the maximum stress and strain are $0.87MPa$ and 1.4, respectively.

One more issue about the material needs to be mentioned. Based on the research of Lin et al. [75], the curing depth is an increasing function of light dose, but it is a decreasing function of the oxygen concentration, viscosity effect, and oxygen external supply rate. The material is not transparent, and the maximum depth is 0.6mm in this paper. Lee et al. [76] showed that photoinitiator played a significant role in controlling the quality and performance of the formed gel network with special regard to thickness of cured layers. The material is not transparent either. The maximum depth is 2.5mm. Aparna Boddapati [77] found that the depth is a versatile model that is a function of factors such as cure depth, incident intensity and initiator concentration. The material is not transparent. It mixed different components to get the polymer, but the color is unclear. The maximum thickness is 0.3mm. Based on these conclusion, curing depth is a function of incident intensity, initiator concentration and time. In order to make sure liquid material in the cavity is completely cured, increasing initiator and incident intensity, and at the same time prolonging the curing time will also play a positive role upon curing depth.

Because the material is brandy new on the market, more investigation should be done about it. One 5cm-side-length cube with 1cm small cube inside was printed. After fabrication, post-curing was conducted. Afterwards, the cube was cut into two halves, finding the small cube was still polymerized.

3.3 Sufficient Condition

Assume the configuration of the final desire is a set named D, that contains n foldable patches $FP_i(i = 1,2,\cdots n)$. The relation of D and FP_i should meet the desire before folding, the planar is called as P. Every patch would be written as $P_i(i = 1,2,\cdots n)$. Also, the same condition has to be satisfied: $P \subset \bigcup_{i=1}^{n} P_i$ For each patch is taken as rigid. From P to D, it should exist a transformation T. If discretize the transformation into infinite interval, the

initial and final states are noted as 0 and 1, therefore, the relationship between D and P should satisfy $T(0) = P$ and $T(1) = D$.

For each planar patch P_i and the corresponding FP_i, the transformation can be expressed as $T_i(P_i) = FP_i$. On the other hand, the inverse transformation T_{-1}^{-1} as well should have the relationship as follows $T_{-1}^{-1}(FP_i) = P_i$.

For any two patches P_i and P_j, the intersection of $P_i \cap P_j = (i, j = 1, 2 \cdots n$ and i $\neq$ j). Additionally, the inverse relationship would also be valid. Similarly, the $FP_i \cap FP_j = (i, j = 1, 2 \cdots n$ and $i \neq$ j).

Chapter 4

Methodology

To obtain 3D shapes from the fabrication of 2D sheets of 'non-smart' materials, our approach is to leave part of the model uncured during the printing process and utilize the post-curing process to set its 3D shape. To realize this approach, the 2D sheets must be designed with the capabilities to:

1. Trap the resin inside the model during the printing process.
2. Contain the resin in place without leakage during deformation.
3. Resist deformation after post-curing.

Since our work is motivated by origami where deformation occurs only at the fold lines, research was performed on the hinge design. Referring to the illustration shown in Fig. 4.1, given an origami pattern with defined fold lines and angles, the fold lines are converted to 3D hinges. We propose to include a cavity (in yellow) for every hinge such that it contains uncured resin after the 2D sheet is fabricated. The hinges are designed to facilitate folding in a particular direction, similarly to creating creases in a paper before folding. In this case, they are directly 3D-printed, meaning there is no need to manually and individually crease each fold to obtain the final shape, an overall actuation can be used to automatically fold all hinges. Once the 2D sheet is folded, a post-curing process is done to fully cure the material as well as the resin inside the cavity. After the resin is cured (in orange), it will try to retain its folded shape, and thus the final 3D shape will be obtained.

Mathematically speaking, when the hinge is folded by an external actuation (Fig. 4.1(c)), it has an internal reaction moment M_R. After the resin in the cavity is cured (Fig. 4.1(d)) and the external actuation is released, the reaction moment M_R then acts as the external load M_{ex} to deform the newly cured material, which in turn generates an internal reaction moment M_{in}

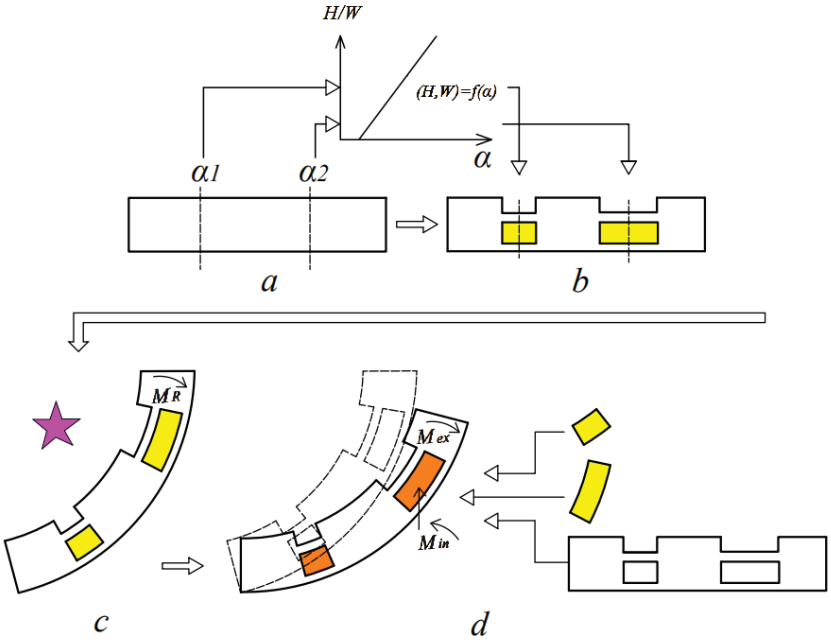

FIGURE 4.1: An illustration of the proposed process. a) Initial origami pattern with two hinges of bending angles α_1 and α_2. b) Through a calibrated mathematical model, the hinge parameters are obtained and the hinges are designed accordingly with cavity to contain uncured resin. c) External moment is used to deform the material, and post-curing is conducted to cure the resin inside the cavity. d) The shape is maintained in folded shape even after the external moment is removed, as a balance between the material cured in different steps.

in the cavity region, until they balance out each other and reach equilibrium, i.e., $M_{ex} = M_{in}$. Therefore there are two methods to retain the actuated state as much as possible after post-curing. One way is to maximize the moment M_{in} in the cavity region, and the other way is to minimize the moment M_R in the rest of the part. In Sec. 4.1, the design and development to address all the aforementioned requirements are presented.

4.1 Hinge Design

To trap uncured resin in the model, a cavity is introduced into each hinge design. The cavity is fabricated as shown in Fig. 3.1, and it is important that the cavity can keep the resin inside during the shaping process. That is, the cavity cannot be raised higher than the resin level during printing, and the weight of the resin inside the cavity should be small enough so that the atmospheric pressure can keep them in place. Similar to the principle used in barometer,

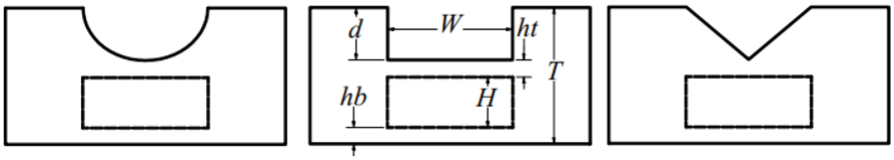

FIGURE 4.2: The sectional schematic of three hinges: elliptical, square, and triangle. T – thickness of the material. H – height of the cavity. hb – thickness of the cavity bottom. ht – thickness of the cavity top. W – width of the hinge. d – depth of the hinge notch.

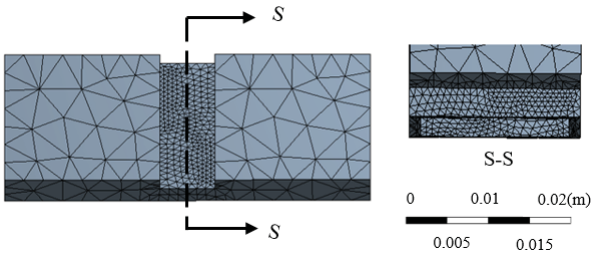

FIGURE 4.3: The simulation mesh of square hinge.

the pressure in the cavity increases with height and can be calculated as:

$$P = \rho g h \tag{4.1}$$

where P is the atmospheric pressure, ρ is the density of resin, g is the gravity constant, and h is the height of cavity above the resin level.

Given $P = 101,325Pa$, $\rho = 1100kg/m^3$, and $g = 9.8m/s^2$, the maximum height of cavity that can keep the uncured resin in place is $9.4m$. Since it is far much larger than the normal sizes that are fabricated using DLP 3D printing, this limiting factor would never be reached. However, this does not validate the method completely as the bottom surface of the cavity must also be able to retain the resin inside. From various test during the calibration of this method, a cavity height of over $10mm$ was achieved with no issues. As such, for the range of DLP origami being $2-4mm$, the material and process is acceptable. The absolute limits of the cavity height are not presented and would be dependent on the material selected.

Flexure hinges have been used to replace other bearings and universal joints, because they are simple, compact, lightweight, and have low friction. Different designs have been applied in medical, micro and nano scale applications, in which elliptical, square, and triangle hinges are the most common geometries [78] (see Fig. 4.2). From these three geometries, the goal is to determine the hinge which can reach the largest folding angle without leakage of resin from the cavity during folding. On one hand, to maximize the folding angle, it is to minimize

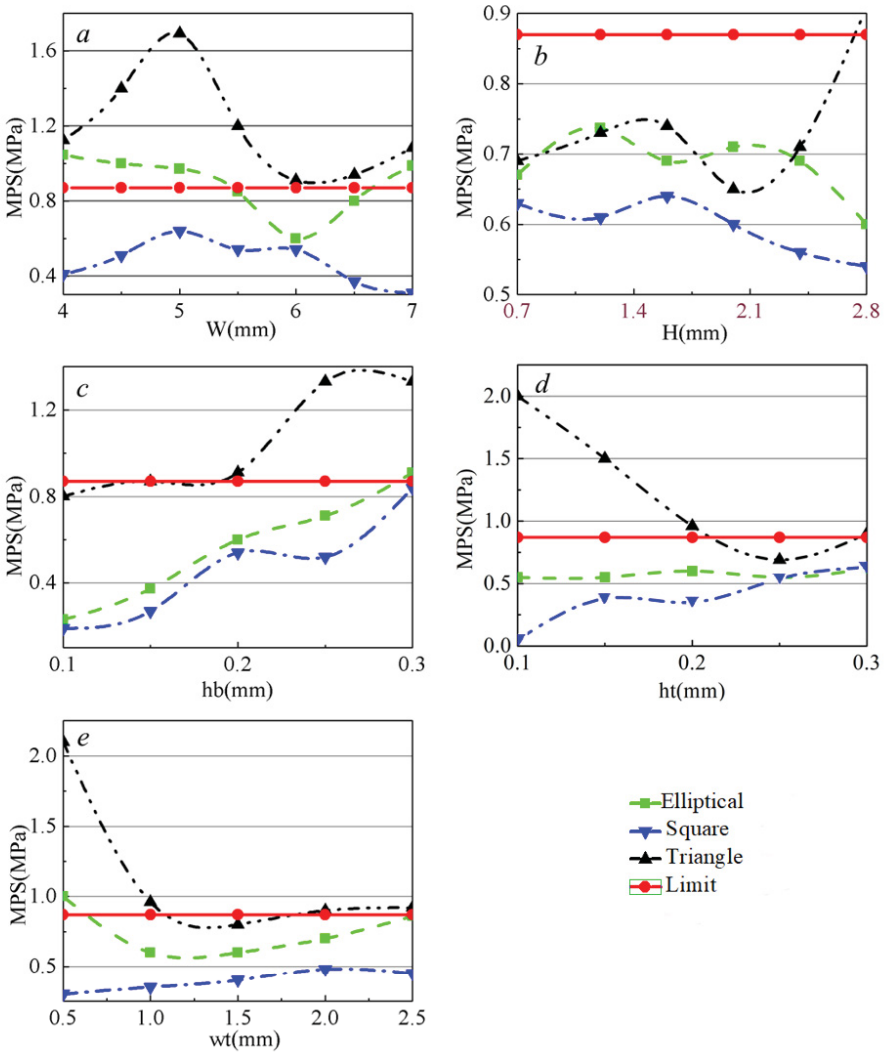

FIGURE 4.4: Influence of W, H, hb, ht and wt on MPS

the reaction moment M_R. For that reason, it is needed to minimize the material experiencing the initial deformation and maximize the volume of the cavity. Referring to Figs. 4.2 and 4.3, besides the thickness of the hinge (T) that is given as an input, there are five other parameters. They are listed as follows; the opening of the hinge (W); the height of cavity (H); the top and bottom walls of cavity (ht, hb); and the side walls of cavity (wt). The parameters hb and ht are dependent on H and should be minimized, while wt is the another parameter the intuitively should be minimized to allow for a larger cavity. On the other hand, to prevent leakage and maintain structural integrity, the maximum stress should not be higher than the ultimate stress throughout the process. In other words, the objective of the hinge design is to minimize the material around the hinge and maximize cavity size which minimizes reaction moment while maintaining a maximum stress of the cavity walls less than the ultimate strength of the

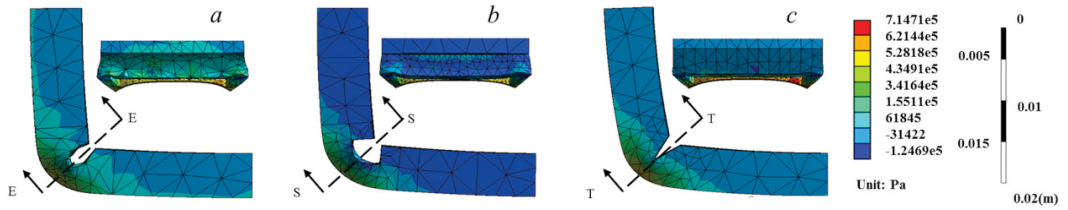

FIGURE 4.5: The comparison of different hinges with parameters $W = 6mm, H = 2.8mm, ht = 0.2mm, hb = 0.2mm, T = 5.5mm$. a) elliptical hinge and its section view. b) square hinge and its section view. c) triangle hinge and its section view.

material.

To find out which geometry has the lowest maximum stress during folding, models of the three shapes are built and simulated in ANSYS. The length, width, and height of the models are $40mm$, $15mm$, and $5.5mm$, respectively. The thickness of the 2D sheet is $T = 5.5mm$ and the depth of the hinge is $d = 2.3mm$. Tetrahedral mesh is used, and the subdivision at the hinge area is doubled to achieve higher accuracy (see Fig. 4.3). There are in total about $10k$ elements and $7k$ nodes in the simulation mesh. One end of the model is fixed and a remote displacement is applied on the other end. Since the deformation is significant, large deflection is enabled in the analysis setting. The calibrated data from Fig. 3.3 is imported to ANSYS for the simulation. The hyper-elastic model used is the Mooney-Rivlin 5 parameter model.

The failure of materials can be determined using the maximum stress criterion, which assumes that a material fails when the maximum principal stress (MPS) in a material element exceeds the uniaxial tensile strength of the material. Therefore, the MPS is reported here, and the material will fail if it exceeds $0.87MPa$ (from Fig. 3.3). Different values for each of the five parameters are tested to obtain their individual contributions on the stress distribution, the MPS of the geometries are reported in Fig. 4.5. By comparing with the 'Limit' of $0.87MPa$, it can be seen that the 'Triangle' hinge often has a stress higher than the ultimate stress, and although the 'Elliptical' hinge has some safe configurations, the choices are limited. Among them, the 'Square' hinge consistently has the lowest MPS and is below the limit in every case. The results are further verified by the visualization shown in Fig. 4.5, for a particular set of parameters. It reveals that under the same folding, the square hinge bends like a bar element with a lower curvature compared to the elliptical and triangular hinges. From this we can extrapolated that a sharper hinge geometry will result in a higher MPS. From the Fig. 4.5(a),

TABLE 4.1: Summary of the hinge variables.

T(mm)	*d(mm)*	*ht(mm)*	*hb(mm)*	*wt(mm)*
5.5	*2.3*	*0.2*	*0.2*	*1.5*

(b) and (c), the MPSs can be seen as located below the cavity where the greatest elongation occurs, and the values are $0.60MPa$, $0.54MPa$ and $0.91MPa$ for the elliptical, square and triangular hinges, respectively, all stresses being in the tensile direction.

It is concluded that the square hinge is the most suitable geometry for our purpose, and it is selected in this study. It allows a wider range of design parameters which translates directly into a wider range of desired folding angles. The objective is to maximize the volume of the cavity and thus the moment M_{in} which helps maintain the desired 3d shape. The opening of the hinge W is set as at most $6mm$ and the top/bottom walls of cavity are set as $ht = hb = 0.2mm$, which are the maximum horizontal length and the minimum thickness of a support bridge that can be stably fabricated with the 3D printer being used. The depth of the hinge d is set based on the geometric assumption that the natural axis is located at the bottom of the opening (see Fig. 4.2). When the top of the hinge is closed by W, the bottom of the hinge will be elongated (l) according to the ratio between the heights, and it should be smaller than the elongation at break (ξ), i.e.,

$$\frac{l}{W} = \frac{T-d}{d} \leq \xi \tag{4.2}$$

where $\xi = 1.4$. Given the thickness of the 2D sheet is $T = 5.5mm$, the depth of the hinge d needs to be greater than or equal to $2.3mm$, this paper uses $d = 2.3mm$. Thus, the height of cavity H is at most $2.8mm$. Because ht and hb are dependent on H, and wt is constant, the two variables which show the highest affect on the cavity volume and selected for the control of the folding angle are W and H. The variables which are kept constant for the hinge designs have their values expressed in Table 4.1.

4.2 Comparison between simulation and theoretical model

It can be seen from Sec. 4.1 that MPs are of great importance in folding, therefore, in order to verify the simulation result, a theoretical model is built up to compare the maximum principal stress with ANSYS. Based on bending theory, the maximum stress can be expressed as

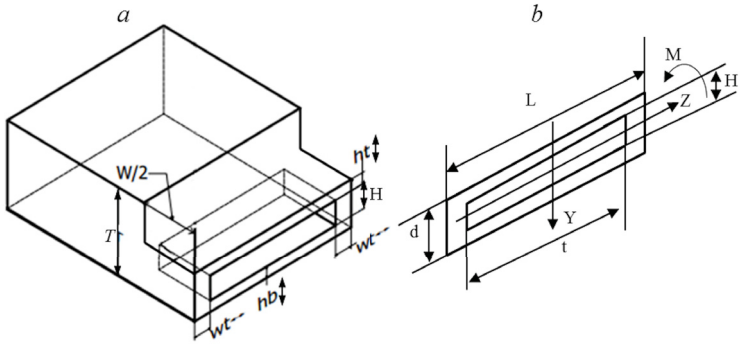

FIGURE 4.6: a) sketch of semi-square hinge. b) cross-section of the hinge part.

TABLE 4.2: MPs comparison between ANSYS and theoretical model

$ht(mm)$	$hb(mm)$	$W(mm)$	$H(mm)$	$M_z(N\times m)$	ANSYS(MPa)	Theoretical(MPa)
0.2	0.2	4	0	10	0.54	0.57

below [79]:

$$\sigma = -\frac{M_z \times y}{I_z} \tag{4.3}$$

In simulation, there is no liquid resin in the cavity, and the neutral plane is a little under the middle plane of the cavity. Additionally, the bottom layer will deform towards the cavity. Thence, y is roughly taken as 1.1mm. I_z could be derived by $I_z = Ld^3/12 - tH^3/12$. Take $L = 15mm, t = 12mm, H = 3.2mm, H = 2.8mm$ as an example, by which I_z can be gotten $I_z = 19.008mm^3$.

Thus, Table 4.2 is designed to compare the accuracy in ANSYS and theoretical model. It can be seen from Table 4.2 that MPs in ANSYS and the theoretical model are 0.54 MPa and 0.57 MPa separately.

4.3 Modeling and design of folding angle

Hinge parameters W and H dictate the final folding angle of a hinge, thus the inverse problem, which is more intuitive for design, would be to select a folding angle which dictates the parameters. The relationship between the parameters and folding angle is obtained through a heuristic approach. Initially we populate the design space through the forward method with predetermined values for W and H, obtain the resulting folding angles, and build a

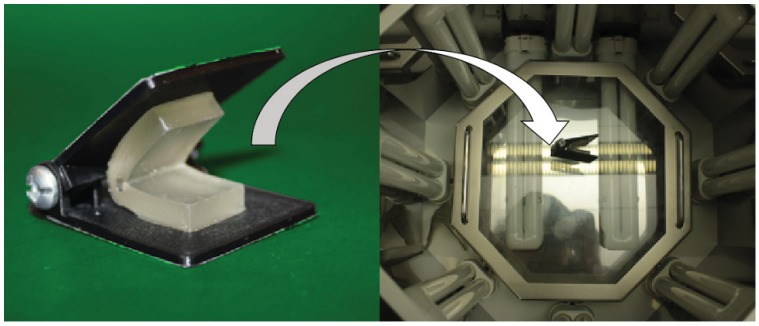

FIGURE 4.7: Folding device used for the calibration of folding angles and the while setting is put in the curing box for post-curing.

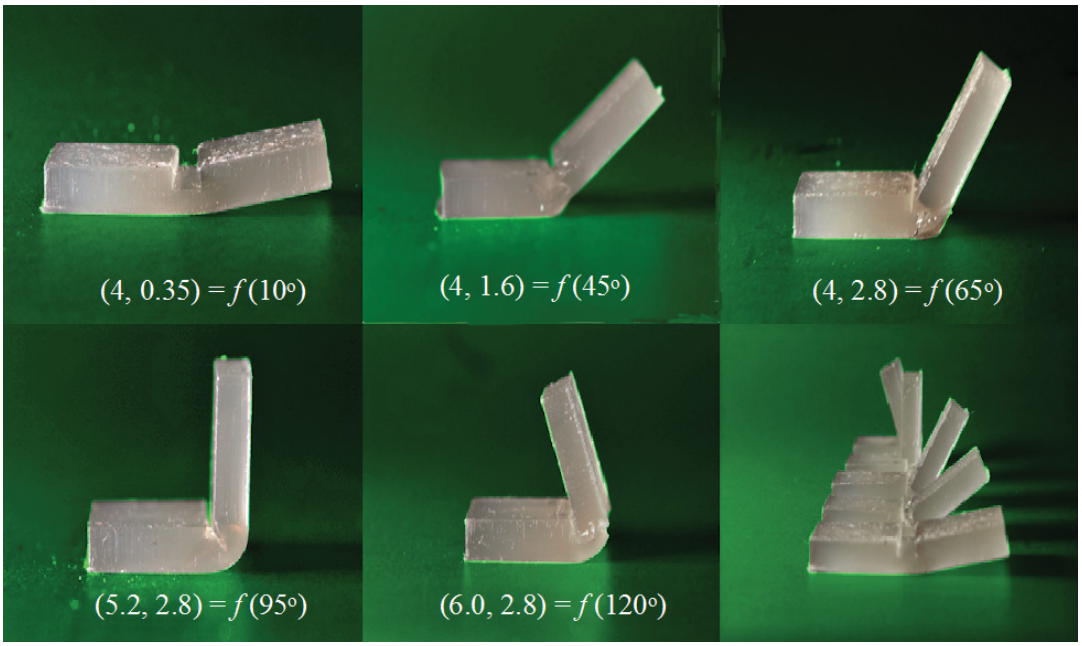

FIGURE 4.8: The bending angles α can be controlled by different values of (W,H). W is the width of hinge, and H is the height of cavity. The equation is in the form of $(W,H) = f(\alpha)$.

mathematical model to describe the relationship.

$$(W,H) = f(\alpha) \tag{4.4}$$

Before the design of experiment, a few trials have been made to identify the maximum folding angle. The largest and the most repeatable angle was achieved when $W = 6mm$, $H = 2.8mm$, resulting in a folding angle of 120°. Decreasing the value of W results in a direct decrease in folding angle. However, there is a limit when W is less than $4mm$ that results in interference in the opening of the hinge which hinders folding. Therefore, we apply two variables to the control of folding angle for two different instances. When the angle is

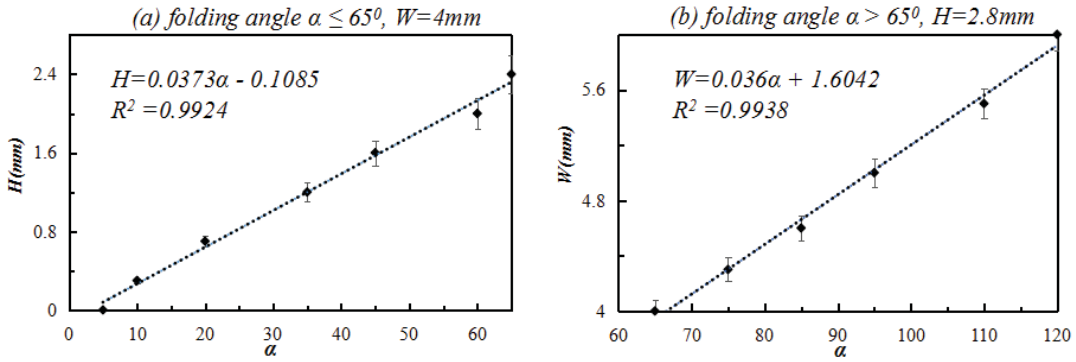

FIGURE 4.9: Linear regression of experimental data to calibrate the folding angle with the hinge parameters. Left: the cavity height (H) against small folding angle ($\alpha \leq 65°$). Right: the hinge width (W) against large folding angle ($65 \leq \alpha \leq 120°$).

large, it is controlled by the hinge width W, and the cavity height H is set to its maximum. When the angle is small and W cannot be further reduced, we modify H to control the angle, with W set to its minimum (i.e., $4mm$). Therefore, the experiments are designed based on W and H, in which W is ranging from $4mm$ to $6mm$, and H is ranging from $0mm$ to $2.8mm$, with a step size of $0.4mm$.

TABLE 4.3: Folding test data based on different (H, α)

$ht(mm)$	$W(mm)$	$H(mm)$	$H\alpha(°)$	$\alpha(°)$
0.2	4	0	140	5
0.2	4	0.35	140	10
0.2	4	0.7	140	20
0.2	4	1.2	140	35
0.2	4	1.6	140	45
0.2	4	2.4	140	60
0.2	4	2.8	140	65

TABLE 4.4: Folding test data based on different (W, α)

$ht(mm)$	$hb(mm)$	$H\ (mm)$	$W(mm)$	$H\alpha(°)$	$\alpha(°)$
0.2	0.2	2.8	4	140	65
0.2	0.2	2.8	4.4	140	75
0.2	0.2	2.8	4.8	140	85
0.2	0.2	2.8	5.2	140	95
0.2	0.2	2.8	5.6	140	110
0.2	0.2	2.8	6.0	140	120

All samples have the size of $40mm \times 15mm \times 5.5mm$, and each configuration is repeated five times. They are fabricated based on the manufacturing process outlined in Sec. 3.1. The only difference is that before the post-curing step, the samples are folded with a simple folding device (see Fig. 4.7), and the assembly is put a UV curing station. The device havs two

movable plates that are assembled by two screws which allows the adjustment of the opening angle. Since the final shape is a balance between the materials cured in different steps, to have an bending angle α, the holding angle $H\alpha$ to set the shape with the folding device needs to be larger than α. This holding angle could also be another design parameter to control the final angle. However, changing the holding angle will complicate the manufacturing and assembly processes and add another degree of freedom which is not necessary to achieve the desired angles. In addition, different values for the holding angle were tested and it was showed that when the holding angle was much greater than the desired angle, its effect was negligible. For the sake of creating an unified process, we fix the holding angle to 140° in this calibration. The experimental tabulated results can be seen in the Table 4.3 and Table 4.4. Some final shapes of the samples are shown in Fig. 4.8, and the experimental results are plotted in Fig. 4.9 with two graphs: H against α, and W against α. Since the data sets are almost linear, a linear regression is used to model each relationship. The resultant R^2-value is 0.99. As a result, the mathematical model to obtain the hinge parameters (W and H) for a given bending angle is defined as

$$(W,H) = f(\alpha) = \begin{cases} (0.036\alpha + 1.6042,\ 2.8) & \alpha > 65^\circ \\ (4,\ 0.0373\alpha - 0.1085) & \alpha \leq 65^\circ \end{cases} \tag{4.5}$$

This exactness of this model has been obtained for the material we are using, as such different resins will have to be calibrated and utilize their own material properties for the parameter limits and method described.

The reason why M_z is not taken as one parameter in calibration is present as below:

From the view of design and manufacturing process, it is relatively easy to modify the CAD model rather than manufacturing process (moment provided). Additionally, it is easy to realize automation without using moment as a parameter, because the moment in each hinge is not that easy to control.

What's more, in experiment, it is found that the moment has no obvious relationship with final folding angle in the large range. When switch to the small range, the moment used has relationship with final angle, but trying to control moment at each specified hinge will complex the manufacturing process.

It will be interesting to design an origami in which the moment is known at designated

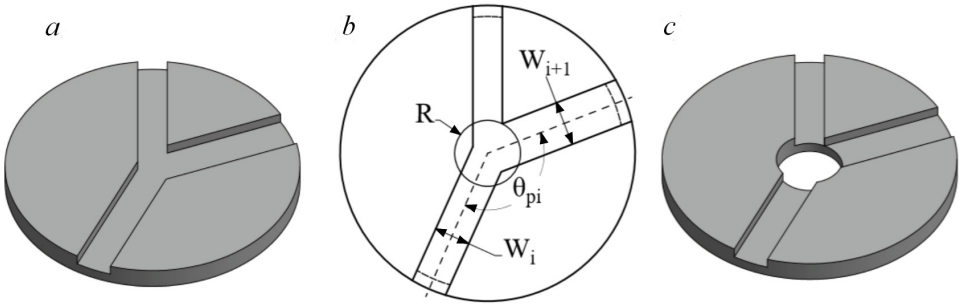

FIGURE 4.10: Interference of adjacent hinges. a) 3D model when adjacent hinges meet up. b) 2D sketch of adjacent hinges. c) 3D model with residual hole.

hinge in advance when overall actuation is applied. Based on the moment and the expected folding angle, a hinge design is raised, which will be my future work.

4.4 Interference between hinges

In an origami pattern, intersection at a vertex may occur when multiple hinges are present, this causes interference and hinders the desired result, especially as the thickness of the material increases, seen in Fig. 4.10(a). To eliminate the interference, a common practice is to introduce a hole at the vertex to decouple the hinges [44].

Referring to the $2D$ sketch Fig. 4.10(b), the hole should be large enough such that the hinges do not have any overlap. Assume i and $i+1$ are two adjacent hinges with widths W_i and W_{i+1}, respectively. The two hinges are intersecting at a vertex O, and the angle between the two hinges is θ_{pi}. Because W_i and W_{i+1} are obtained from Sec. 4.3, it is possible to derive the minimum radius of residual hole in terms of W_i, W_{i+1} and θ_{pi}, applying the arc length formula:

$$R_i = (W_i + W_{i+1})/2\theta_{pi} \tag{4.6}$$

If there are more than two hinges intersecting at a vertex, the radius of hole should be the maximum value among all the pairs of neighbouring hinges. Finally Fig. 4.10(c) shows the modified 3D model.

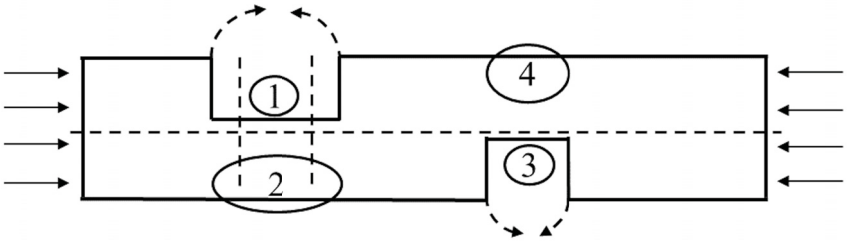

FIGURE 4.11: Reactions between multi-hinges.

4.5 From one single hinge to multi-hinge design

Origami is much easy to be folded along the weak spots, like notches, grooves on origami. The weak spots on the surface is served as guidance to lead the folding.

Additionally, it is because of stress concentration that origami will fold towards hinge side. Locally, only from the area of hinge (between two dash lines in Fig. 4.11), the stress distribution is the same. But from the view of whole origami pattern, if origami is folding towards the opposite side of the hinge, the material will accumulate in the bending area (area 2 and 4), and the piled material will resist the deformation once bending is started, which will dramatically decrease the final folding angle.

Furthermore, one-side hing design will facilitate manufacturing automation. For multiply hinges, the average neutral plane is beneath the hinge (horizontal dash line in Fig. 4.11). If an overall actuation is applied in some way, the origami pattern will fold towards the hinge side, because there is a notch, and the stiffness could be regarded as zero, whilst the opposite side of hinge is solid with relatively higher stiffness, which is harder to bend compared with hinge side. For example in Fig. 4.11, when an overall actuation (distributed load) is applied on both sides, the hinge side is inclined to fold firstly along the curved arrow because of lower stiffness in area 1 and 3 compared with area 2 and 4. Considering the manufacturing automation, the one-side hinge design is prone to realize automation in industry. What needs to mention is that the actuation should be controlled strictly, because area 2 and 4 would also bend if the actuation is large enough.

To sum it up, to fold in the opposite direction is one choice, but needs extra actuation.

Chapter 5

Experimental Results

With the developed hinge design, fabrication method, and mathematical model, this section will apply them to test the methodology and demonstrate some possible usages. The same terminology in origami will be used to describe the patterns. For example, a hinge can be designed as a valley fold or a mountain fold. If it is a valley fold, the opening of hinge is pointing upward with respect to the viewing direction, otherwise the opening points downward and is located at the back of the pattern. Unless otherwise stated, the thickness of samples in the experiments are designed as $T = 5.5mm$.

5.1 Quasi-one-dimensional strips

One-dimensional (1D) strips are relatively simple in topology, but they have many applications, such as robotics, mechanical springs, architectural design or aesthetics [2]. They are used as the first example the verify the proposed method. Two letters – 'C' and 'W' – are selected for fabrication, where 'C' has folds in one direction and 'W' has folds in both directions. Both are approximated by a 1D strip with three hinges, the CAD models of which are shown in Fig. 5.1(a) and (b). The length and width of the strips are $100mm$ and $15mm$, respectively. All three hinges of the letter 'C' are valley folds with a designed folding angle of 75° (valley), which in turn give the hinge parameters $W = 4.4mm$ and $H = 2.8mm$. For the letter 'W', the folding angle of the middle hinge is designed as 100° (mountain), and the angles of the side hinges are 120° (valley). This gives the opening of middle hinge pointing downward, with the parameters $W = 5.4mm$ and $H = 2.8mm$, and the opening of side hinges upward, with the parameters $W = 6.0mm$ and $H = 2.8mm$.

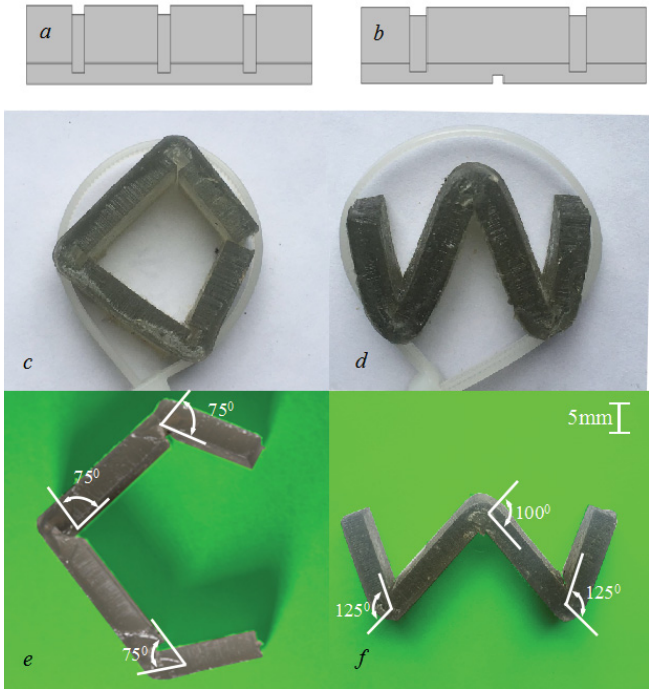

FIGURE 5.1: One-dimensional strips. (a - b) The 3D models of the letters 'C' and 'W'. (c - d) The shape-setting is done by a cable tie. (e - f) The final shapes after the cable tie is removed.

Since the hinges are designed to facilitate folding in the desired direction, the shape-setting before post-curing can be as simple as using a cable tie to circle up the strips, and they are automatically formed into the shape of letters correspondingly, as shown in Fig. 5.1(c) and (d). The actuation using a cable tie is the same for both models, and the diameter can be adjusted through stretching the rope. Although the holding angles for the hinges may not be the same under this overall actuation, the effect is negligible as long as they are larger than the desired angle like discussed in Sec. 4.3. After the structures are deformed by the cable tie, the whole thing is put into the LC-3D Print Box for the post-curing. The final shapes obtained are shown in Fig. 5.1(e) and (f). It can be seen that even after the rope is removed, the structures can stay in the deformed shapes on their own. All the hinges in the letter 'C' are maintained with an angle around 75° as designed, and similarly the middle hinge of the letter 'W' is maintained in an angle around 100°. There is a slight difference for the side hinges of 'W', and they have a final angle around 125° (designed 120°), which might be caused by the manufacturing inaccuracy and the overstretching. We have also tried to press the structures flat, and they can still return to the configurations of 'C' and 'W'.

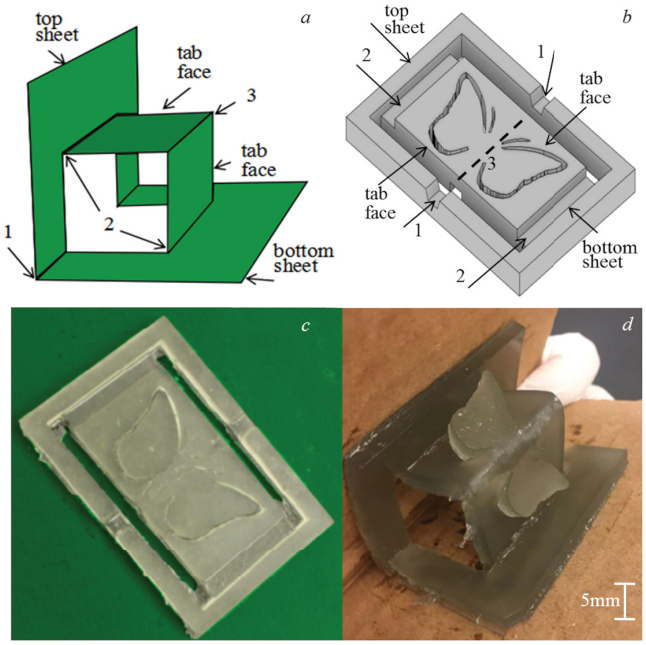

FIGURE 5.2: Pop-up. a) The mechanism of pop-up using parallel folds. b) The CAD model of a pop-up design with a butterfly profile. c) The printed 2D sheet. d) A folder is used to fold the sheet and make the butterfly being popped out.

5.2 Pop-ups

Pop-ups are the designs that arise from 2D configuration into 3D by simple folding like opening a page, and a common example is a pop-up book or card. Pop-ups come in different categories, depending on their geometry, including parallel folds, angle folds, and the combinations of them. For example, in parallel folds, the linkages are connected with the shape like a parallelogram (see Fig. 5.2(a)), and can be best represented as a four-bar linkage. By keeping the bottom sheet flat on the ground, moving the top sheet will change the angle of the middle hinge (labelled 1). Due to the parallelism, the opposite tabs will move accordingly and pop out from the original plane. This mechanism is employed with the proposed method in this paper to produce final 3D shapes with a simple folding method.

A profile of butterfly is designed and engraved into the tabs as shown in Fig. 5.2(b). The whole size of the model is $100mm \times 60mm$. To simulate cuts, a $5mm$ gap is added between the outer frame and the tab. There are five hinges on the sheet: two valley folds (labeled 1) at the middle of the outer frame, one mountain fold (labeled 3) in the center of the tab surface, and two more valley folds (labeled 2) connecting the frame and the tabs. All five hinges are designed to have a folding angle of 90°, which gives $W = 5mm$ and $H = 2.8mm$. The printed

2D sheet is shown in Fig. 5.2(c), and it can be folded using a folding device similar to the one shown in Fig. 4.7. The folding and post-curing procedure are the same as the one used to calibrate the folding angle with hinge parameters. It is worth noting that using this method – pop-up design with the help of a folding device, many different shapes can be fabricated with the same mechanisms, by simply changing the middle pattern.

In this example, when the 2D sheet is actuated, all the hinges fold as designed and it forms a shape of a parallelogram as shown in Fig. 5.2(d). While the tabs connected to the frame by hinges are bent, the engraved profile decouples the butterfly from the tabs, and thus the wings of the butterfly are free to pop out. In addition, since the degree to which the wings pop out from the tabs depends on the angle of the middle hinge, an interesting effect can be seen when the top sheet is moved back and forth – the wings are flapping similar to a flying butterfly. When the final shape is pressed flat, it can automatically return to the folded shape. This characteristic can facilitate packaging and transportation, giving a high packing ratio with 2D sheets and restoring to 3D shapes after unpacking.

5.3 Action origami

Action origami is origami that can have actions after folding. One example is the Oriceps [5], which is an origami-inspired forceps. Conventional forceps often requires assembly from different parts to provide movements. However, the product complexity makes the manufacturing process complicated and the forceps difficult to clean. Due to these problems, Oriceps was proposed to be fabricated by a single sheet, and it can be actuated just like a normal forceps. This can get rid of the complex assembly process, and it is potentially suitable for various scales from macro to micro. It has potential use as surgical forceps because it is compliant and can be easily sterilized.

To demonstrate that the proposed manufacturing method can also produce action origami, the Oriceps design [5] is employed in this paper (see Fig. 5.3(a)). The length and width of the model are 165mm and 83mm, respectively. There are in total twelve hinges (Fig. 5.3(b)): at the side, there are four long ones (1, 2, 3, 4) and four short ones (5, 6, 7, 8), all of which are valley fold; in the middle, there are four hinges, two of which are valley folds (9, 10) and two are mountain (11, 12). The long hinges (1, 2, 3, 4) are designed to have a folding angle 40°, thus the hinge parameters $W = 4mm$ and $H = 1.6mm$. The short hinges (5, 6, 7, 8) are

of folding angle 120° and hinge parameters $W = 6.0mm$ and $H = 2.8mm$. The middle two hinges (9, 10) that are valley folds have a folding angle of $90° - W = 5.0mm$ and $H = 2.8mm$, and the last two mountain folds have an angle of 65° with the hinge parameters $W = 4.0mm$ and $H = 2.4mm$. There are four vertices in the pattern, and they have the same configuration because of symmetry. The angles between hinges (θ_{pi}) at a vertex are 90°, 110°, 70° and 90°, respectively. Therefore, the diameters of the hole is calculated by Eq. (4.6), and the maximum interference results in a $4.09mm$ diameter relief hole.

Limited by the printing size of the 3D printer, the model cannot be fabricated in full scale, so it is uniformly scaled down by half for the physical test. This scaling may affect the shape-retention property, and should be calibrated as well in the future. In this example, the effect is not significant, and the accuracy of folding angles on action origami can be lower. Since all the hinges are designed to bend in the desired direction – pre-folded, the same actuation to actuate the Oriceps can be applied to deform the 2D sheet to the shape-setting configuration, i.e., pulling from the back (see Fig. 5.3(d)). After post-curing, the final shape is kept in the 3D shape as shown in Fig. 5.3(e). It has also been tested by picking up different objects (Fig. 5.3(f-h)), and the results validate the functionality of the Oriceps fabricated by the proposed method. A video showing the oriceps in action is available at https://youtu.be/CTileFPnUAY.

5.4 Bistable Origami

Bistable origami is the structure that has two stable states, while maintaining the configuration of folds the same, i.e., a valley fold is still a valley fold, and vice versa. It can serve as a mechanical memory unit that snaps between two stable states of the folded structure under external stimulus with applications in electronics acting as a switch. One classic bistable origami is the waterbomb base [80], which has only one vertex intersected by six hinges with alternating mountain and valley folds, as shown in Fig. 5.4(a). It is used to test if the bistable property can be replicated by the proposed method.

The 2D model is designed in a hexagon shape, and the length of its sides is $55mm$. Among the six hinges, three are valley folds and three are mountain folds. The valley folds have a folding angle of 75°, which gives the hinge parameters $W = 4.4mm$ and $H = 2.8mm$, and the

mountain folds have an angle of 60°, thus $W = 4.0mm$ and $H = 2.8mm$. The diameter of the hole at the vertex is calculated as $6mm$.

Due to limit of printing size, the model also is scaled down to 3mm thickness before printing. The $3D$ model and detailed wireframe are demonstrated in Fig. 5.4(a). After printing, the 2D sheet is shown in Fig. 5.4(b), and actuated shape is shown in Fig. 5.4(c).

In this example, a fixture is used to set the shape as shown in Fig. 5.4(c).

The final 3D shape is shown in Fig. 5.4(d), which is one of the two stable states. The other one can be obtained by pushing the vertex in the center down to make the structure flat, and after passing the flat state, the structure will snap through to the resultant shape as shown in Fig. 5.4(e). It can be seen that all the hinges are still having the same valley/mountain configuration. This example demonstrates that the part fabricated by the proposed method indeed has the characteristics of origami, and thus it is promising to apply the method for other more complex origami patterns.

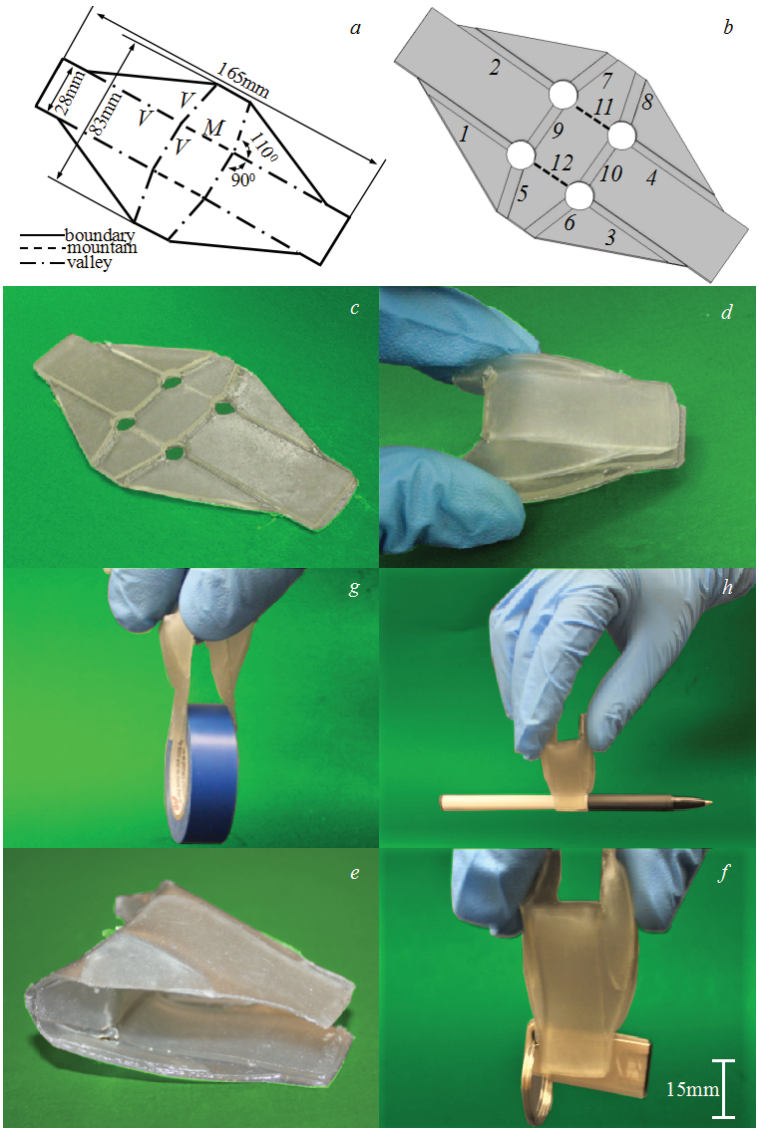

FIGURE 5.3: Forceps. a) 2D sketch of the forceps. b) 3D model of the forceps. c) 2D polymerized sheet of the forceps. d) actuated configuration for post-curing. e) isometric view of the final shape. f) the forceps is holding up a USB key. g) the forceps is holding up one roll of tape (around 20 grams). h) the forceps is holding up a ball pen.

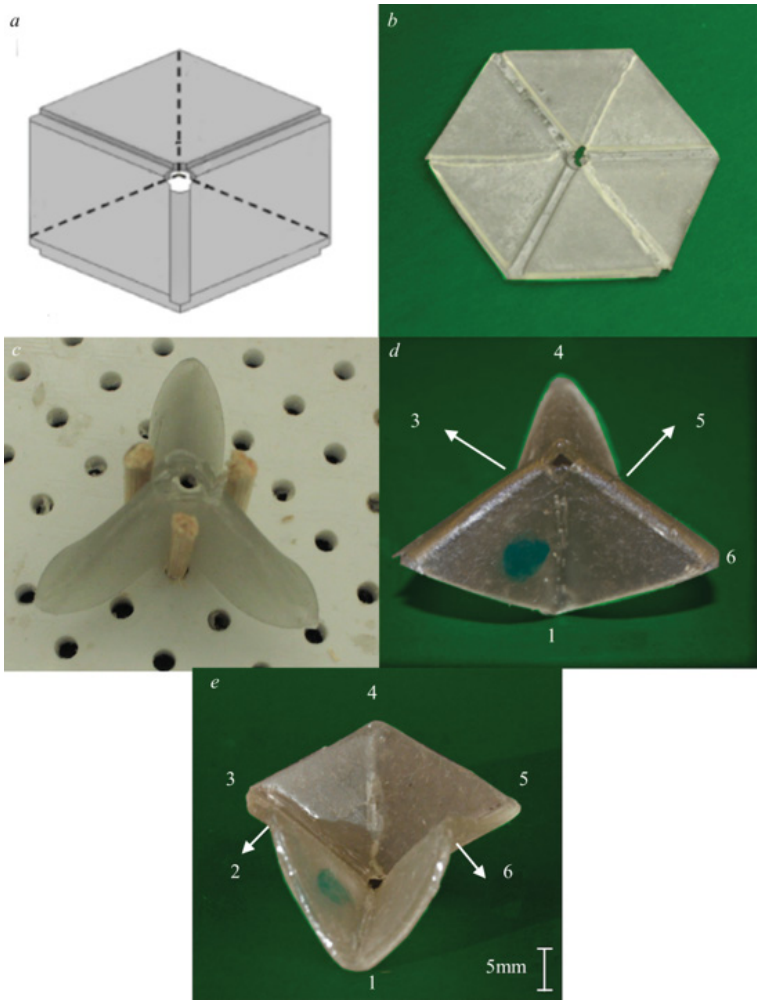

FIGURE 5.4: Waterbomb base. a) 3D model of the waterbomb base – dotted lines indicate the hinges with mountain folds. b) 2D polymerized sheet of waterbomb base. c) Shape-setting configuration before post-curing. d) one stable state of the waterbomb base with the vertex above the flat plane. e) the other stable state with the vertex below the flat plane.

Chapter 6

Conclusion and Future Work

6.1 Conclusion

In the paper, a new manufacturing method based on the digital light processing (DLP) technology is developed to fabricate origami-based components. The objective is to leave parts of the model uncured during the 3D printing step, and then cure them in the post-processing step to set the final shape. In order to test the capability of this method, finite element analysis in ANSYS is conducted to find the most suitable hinge geometry. Due to the relatively lower maximum principal stress, the square hinge is chosen to be modified for our objective. A cavity is incorporated into the hinge design, the goal of which is to trap the uncured resin within the part. A mathematical model is also established to describe the relationship between the hinge parameters (hinge width and cavity height) and the final folding angle. The model is applied to fabricate a few examples with the given final shape to validate the method. Firstly, the one-dimensional strips demonstrate that the method can fabricate multiple hinges at the same time, even if they have different target angles. Secondly, the pop-up butterfly shows that by utilizing the pop-up concept, complex patterns and geometry can be fabricated with the same folding mechanism. Thirdly, an origami-based forceps is printed to prove that the method can produce action origami, which can function after folding. Finally, a bistable waterbomb base is fabricated to reveal that the printed part shares the same characteristics of origami, and thus it is promising to apply the method to other existing origami patterns.

6.2 Future work

Although the results are encouraging, there are some limitations of the method.

- One limitation is the deflects on the 2D sheets after 2D sheet is fabricated by DLP printing. In order to improve that, laser cutting or electropolishing can be used to correct the 2D sheet. Because it is harder to correct the configuration in 3D configuration, the correction is becoming of great significance in 2D stage.

- One other limitation is that the maximum folding angle can be achieved is only 120°, which is not enough to produce sharper features. In the future, we will explore other structure and hinge designs to increase the maximum folding angle. However, since the holding angle needs to be larger than the folding angle, it is not quite possible to fabricate extremely sharp features, like 180° angles. In such cases, other self-locking features may need to be included.

- Another limitation is that under an overall actuation for setting the shape, the moment applied on each hinge might be different, which means that some hinges may experience over-folding while the others are still under-folding. We will investigate the moment at each hinge and modify the hinges, if needed, to realize simultaneous folding.

- In order to get a general relationship of hinge parameters and final folding angle, reduce the number of times needed to solve the equation numerically and give the insight into what might be small parameters that can be ignored or treated approximately, dimensionless analysis is executed. Based on analysis in 4.1, it is known that α(final folding angle) is a function of height of cavity(H), width of opening(W), young's modules(E), actuated moment(M_z), which depicts as α=$f(H,W,E,M)$. According to Buckingham Pi Theorem [81], $\pi 1$ can be expressed as $\pi 1 = W^x E^y M^z H$. After calculation, it is derived as:

$$\pi 1 = \frac{M_z H}{E W^4} \tag{6.1}$$

Similarly, $\pi 2$ can be expressed as

$$\pi 2 = \frac{\alpha M_z H}{E} \tag{6.2}$$

Therefore, the dimensionless relationship can depict as $\pi 1 = f(\pi 2)$. From the relationship, It can be seen that final angle is a function of young's modules, cavity height, hinge width and the bending moment.

In order to verify the non-dimension relationship, a validated experiment is designed as Table 6.1. The objective is to make sure the mapping from $HM_z/(EW^4)$ to $\alpha HWm/E$ is a one-by-one mapping.

TABLE 6.1: Validation on dimensionless analysis

$H(mm)$	$W(mm)$	$M_z(N \times m)$	E(MPa)	$HM_z/(EW^4)$	$\alpha(^\circ)$	$\alpha HWm/E$
0.5	4	10	0.6	33	$\alpha 1$	$6.64\alpha 1$
1.5	5.2	11	0.7	33	$\alpha 2$	$8.12\alpha 2$
2.5	5.8	12	0.8	33	$\alpha 3$	$8.70\alpha 3$
0.5	3.8	10	0.6	40	$\alpha 4$	$6.33\alpha 4$
1.5	4.9	11	0.7	40	$\alpha 5$	$7.74\alpha 5$
2.5	5.5	12	0.8	40	$\alpha 6$	$8.30\alpha 6$
0.5	3.8	10	0.6	40	$\alpha 4$	$6.33\alpha 4$
1.5	4.9	11	0.7	40	$\alpha 5$	$7.74\alpha 5$
2.5	5.5	12	0.8	40	$\alpha 6$	$8.30\alpha 6$
0.5	3.6	10	0.6	40	$\alpha 7$	$5.98\alpha 7$
1.5	4.4	11	0.7	40	$\alpha 8$	$7.32\alpha 8$
2.5	5.2	12	0.8	40	$\alpha 9$	$7.85\alpha 9$

In Table 6.1, the item $HM_z/(EW^4)$ can be set as 33, 40 and 50, and then pick up H, W, M_z during which it needs to make sure $HM_z/(EW^4)$ = 33/40/50. After testing folding angles and comparing these values, if they are all equal, it can prove the dimensionless relationship is valid.

Afterwards, the exact relationship in the format of $y = f(x)$ between the two dimensionless variables can be accessible. For here x is $\alpha HWm/E$, which stands for input, whist y is $HM_z/(EW^4)$ representing output. In order to get the that, Table 6.2 is designed.

TABLE 6.2: Experiment design on dimensionless relationship

Input	*Out put*
30	y1
35	y2
40	y3
45	y4
50	y5

From Table 6.2, a figure can be plotted in $x-y$ coordinates. It is the dimensionless relationship. It could depict in the form of $y = f(x)$ by regression analysis. For the dimensionless relationship, it requires testing on different materials and controlled moment, which will be the future work.

In this thesis, E is known due to only one single material used. α is the goal that is known prior to time. Therefore, only H, W and M_z are left as variables. In order to find one way to establish the design parameters and final angle, two variables can be set as two knowns (for example W and M_z). Through plug these two knowns in the dimensionless relationship, the relationship of H and α expressed in the format of $(H,W,M_z) = f(\alpha)$ [W and M_z are both known] can be obtained.

Bibliography

[1] Pooya Sareh and Simon D Guest. Design of isomorphic symmetric descendants of the miura-ori. *Smart Materials and Structures*, 24(8):085001, jun 2015.

[2] Elissa Morris, Daniel A. McAdams, and Richard Malak. The State of the Art of Origami-Inspired Products: A Review. volume Volume 5B: 40th Mechanisms and Robotics Conference of *International Design Engineering Technical Conferences and Computers and Information in Engineering Conference*, 08 2016. V05BT07A014.

[3] P. A. Jones and B. R. Spence. Spacecraft solar array technology trends. *IEEE Aerospace and Electronic Systems Magazine*, 26(8):17–28, Aug 2011.

[4] Christy D. Saintsing, Benjamin S. Cook, and Manos M. Tentzeris. An Origami Inspired Reconfigurable Spiral Antenna. volume Volume 5B: 38th Mechanisms and Robotics Conference of *International Design Engineering Technical Conferences and Computers and Information in Engineering Conference*, 08 2014. V05BT08A050.

[5] Bryce J. Edmondson, Landen A. Bowen, Clayton L. Grames, Spencer P. Magleby, Larry L. Howell, and Terri C. Bateman. Oriceps: Origami-Inspired Forceps. volume Volume 1: Development and Characterization of Multifunctional Materials; Modeling, Simulation and Control of Adaptive Systems; Integrated System Design and Implementation of *Smart Materials, Adaptive Structures and Intelligent Systems*, 09 2013.

[6] Qi Ge, Amir Hosein Sakhaei, Howon Lee, Conner Dunn, Nicholas Fang, and Martin Dunn. Multimaterial 4d printing with tailorable shape memory polymers. *Scientific Reports*, 6:31110, 08 2016.

[7] Dongping Deng and Yong Chen. Origami-Based Self-Folding Structure Design and Fabrication Using Projection Based Stereolithography. *Journal of Mechanical Design*, 137(2), 02 2015. 021701.

[8] Ying Liu, Julie K. Boyles, Jan Genzer, and Michael D. Dickey. Self-folding of polymer sheets using local light absorption. 2012.

[9] Zeang Zhao, Jiangtao Wu, Xiaoming Mu, Haosen Chen, H. Jerry Qi, and Daining Fang. Origami by frontal photopolymerization. *Science Advances*, 3(4), 2017.

[10] Mohd Rizal Alkahari, Siti Nur Humaira Mazlan, Faiz Redza Ramli, Nurul Ain Maidin, Mohd Nizam Sudin, and Ardzatul Ruziah Zolkaply. Surface finish and mechanical properties of fdm part after blow cold vapor treatment. 2018.

[11] Jiayi Zhu, Julia Chen, Robert Lade, Wieslaw Suszynski, and Lorraine Francis. Water-based coatings for 3d printed parts. *Journal of Coatings Technology and Research*, 12, 07 2015.

[12] Yueqiang Yu, Yanling Guo, Ting Jiang, Jian Li, Kaiyi Jiang, and Hui Zhang. Study on the ingredient proportions and after-treatment of laser sintering walnut shell composites. In *Materials*, 2017.

[13] L.A. Bowen, W.L. Baxter, S.P. Magleby, and L.L. Howell. A position analysis of coupled spherical mechanisms found in action origami. *Mechanism and Machine Theory*, 77:13 – 24, 2014.

[14] Pooya Sareh and Simon D Guest. Design of isomorphic symmetric descendants of the miura-ori. *Smart Materials and Structures*, 24(8):085001, jun 2015.

[15] Kazuko Fuchi, Philip R. Buskohl, Giorgio Bazzan, Michael F. Durstock, Gregory W. Reich, Richard A. Vaia, and James J. Joo. Design Optimization Challenges of Origami-Based Mechanisms With Sequenced Folding. *Journal of Mechanisms and Robotics*, 8(5), 05 2016. 051011.

[16] Levi H. Dudte, E. Vouga, Tomohiro Tachi, and L. Mahadevan. Programming curvature using origami tessellations. *Nature materials*, 15 5:583–8, 2016.

[17] Joseph O. Jacobsen, Brian G. Winder, Larry L. Howell, and Spencer P. Magleby. Lamina Emergent Mechanisms and Their Basic Elements. *Journal of Mechanisms and Robotics*, 2(1), 11 2009. 011003.

[18] Samuel E. Wilding, Larry L. Howell, and Spencer P. Magleby. Spherical lamina emergent mechanisms. *Mechanism and Machine Theory*, 49:187 – 197, 2012.

[19] Nixon Wonoto, Daniel Baerlecken, Russell Gentry, and Matthew Swarts. Parametric design and structural analysis of deployable origami tessellation. *Computer-Aided Design and Applications*, 10(6):939–951, 2013.

[20] Kazuya Saito, Akira Tsukahara, and Yoji Okabe. New Deployable Structures Based on an Elastic Origami Model. *Journal of Mechanical Design*, 137(2), 02 2015. 021402.

[21] sarah-marie belcastro and Thomas C. Hull. Modelling the folding of paper into three dimensions using affine transformations. *Linear Algebra and its Applications*, 348(1):273 – 282, 2002.

[22] Philip R. Buskohl, Kazuko Fuchi, Greg W. Reich, James J. Joo, and Richard A. Vaia. Design tools for adaptive origami devices. In Thomas George, Achyut K. Dutta, and M. Saif Islam, editors, *Micro- and Nanotechnology Sensors, Systems, and Applications VII*, volume 9467, pages 169 – 177. International Society for Optics and Photonics, SPIE, 2015.

[23] Nicolae Lobontiu, Jeffrey S.N. Paine, Ephrahim Garcia, and Michael Goldfarb. Design of symmetric conic-section flexure hinges based on closed-form compliance equations. *Mechanism and Machine Theory*, 37(5):477 – 498, 2002.

[24] Byung-Ju Yi, Goo Bong Chung, Heung Yeol Na, Whee Kuk Kim, and Il Hong Suh. Design and experiment of a 3-dof parallel micromechanism utilizing flexure hinges. *IEEE Transactions on Robotics and Automation*, 19(4):604–612, Aug 2003.

[25] Y. Tian, B. Shirinzadeh, and D. Zhang. Closed-form compliance equations of filleted v-shaped flexure hinges for compliant mechanism design. *Precision Engineering*, 34(3):408 – 418, 2010.

[26] Dongwoo Kang and Daegab Gweon. Analysis and design of a cartwheel-type flexure hinge. *Precision Engineering*, 37(1):33 – 43, 2013.

[27] Qiang Li, Cunyun Pan, and Xiaojun Xu. Closed-form compliance equations for power-function-shaped flexure hinge based on unit-load method. *Precision Engineering*, 37(1):135 – 145, 2013.

[28] Yanding Qin, Bijan Shirinzadeh, Dawei Zhang, and Yanling Tian. Compliance modeling and analysis of statically indeterminate symmetric flexure structures. *Precision Engineering*, 37(2):415 – 424, 2013.

[29] Nicolae Lobontiu and Matt Cullin. In-plane elastic response of two-segment circular-axis symmetric notch flexure hinges: The right circular design. *Precision Engineering*, 37(3):542 – 555, 2013.

[30] Nicolae Lobontiu. Compliance-based matrix method for modeling the quasi-static response of planar serial flexure-hinge mechanisms. *Precision Engineering*, 38(3):639 – 650, 2014.

[31] R. Friedrich, R. Lammering, and T. Heurich. Nonlinear modeling of compliant mechanisms incorporating circular flexure hinges with finite beam elements. *Precision Engineering*, 42:73 – 79, 2015.

[32] Xuejun Wang, Changli Liu, Junjie Gu, and Wenjun Zhang. A parametric model for rotational compliance of a cracked right circular flexure hinge. *International Journal of Mechanical Sciences*, 94-95:168 – 173, 2015.

[33] Simona Noveanu, Nicolae Lobontiu, Joshua Lazaro, and Dan Mandru. Substructure compliance matrix model of planar branched flexure-hinge mechanisms: Design, testing and characterization of a gripper. *Mechanism and Machine Theory*, 91:1 – 20, 2015.

[34] Farid Parvari Rad, Rocco Vertechy, Giovanni Berselli, and Vincenzo Parenti-Castelli. Analytical compliance analysis and finite element verification of spherical flexure hinges for spatial compliant mechanisms. *Mechanism and Machine Theory*, 101:168 – 180, 2016.

[35] Miao Yang, Zhijiang Du, and Wei Dong. Modeling and analysis of planar symmetric superelastic flexure hinges. *Precision Engineering*, 46:177 – 183, 2016.

[36] Min Liu, Xianmin Zhang, and Sergej Fatikow. Design and analysis of a multi-notched flexure hinge for compliant mechanisms. *Precision Engineering*, 48:292 – 304, 2017.

[37] Lei-Jie Lai and Zi-Na Zhu. Design, modeling and testing of a novel flexure-based displacement amplification mechanism. *Sensors and Actuators A: Physical*, 266:122 – 129, 2017.

[38] Lin Cao, Allan T. Dolovich, Ang Chen, and Wenjun (Chris) Zhang. Topology optimization of efficient and strong hybrid compliant mechanisms using a mixed mesh of beams and flexure hinges with strength control. *Mechanism and Machine Theory*, 121:213 – 227, 2018.

[39] Sebastian Linß, Philipp Gräser, Thomas Räder, Stefan Henning, René Theska, and Lena Zentner. Influence of geometric scaling on the elasto-kinematic properties of flexure hinges and compliant mechanisms. *Mechanism and Machine Theory*, 125:220 – 239, 2018.

[40] Jianwei Wu, Yin Zhang, Shuai Cai, and Jiwen Cui. Modeling and analysis of conical-shaped notch flexure hinges based on nurbs. *Mechanism and Machine Theory*, 128:560 – 568, 2018.

[41] Zhong Chen, Xiaomeng Jiang, and Xianmin Zhang. Damped circular hinge with integrated comb-like substructures. *Precision Engineering*, 53:212 – 220, 2018.

[42] Christina L. Randall, Yevgeniy V. Kalinin, Mustapha Jamal, Aakash Shah, and David H. Gracias. Self-folding immunoprotective cell encapsulation devices. *Nanomedicine: Nanotechnology, Biology and Medicine*, 7(6):686 – 689, 2011.

[43] Bryce J. Edmondson, Landen A. Bowen, Clayton L. Grames, Spencer P. Magleby, Larry L. Howell, and Terri C. Bateman. Oriceps: Origami-Inspired Forceps. volume Volume 1: Development and Characterization of Multifunctional Materials; Modeling, Simulation and Control of Adaptive Systems; Integrated System Design and Implementation of *Smart Materials, Adaptive Structures and Intelligent Systems*, 09 2013. V001T01A027.

[44] C. D. Onal, R. J. Wood, and D. Rus. An origami-inspired approach to worm robots. *IEEE/ASME Transactions on Mechatronics*, 18(2):430–438, April 2013.

[45] S. Miyashita, L. Meeker, M. Goldi, Y. Kawahara, and D. Rus. Self-folding printable elastic electric devices: Resistor, capacitor, and inductor. In *2014 IEEE International Conference on Robotics and Automation (ICRA)*, pages 1446–1453, May 2014.

[46] S. Felton, M. Tolley, E. Demaine, D. Rus, and R. Wood. A method for building self-folding machines. *Science*, 345(6197):644–646, 2014.

[47] Kate Malachowski, Mustapha Jamal, Qianru Jin, Beril Polat, Christopher J. Morris, and David H. Gracias. Self-folding single cell grippers. *Nano Letters*, 14(7):4164–4170, 2014. PMID: 24937214.

[48] S. Miyashita, S. Guitron, M. Ludersdorfer, C. R. Sung, and D. Rus. An untethered miniature origami robot that self-folds, walks, swims, and degrades. In *2015 IEEE International Conference on Robotics and Automation (ICRA)*, pages 1490–1496, May 2015.

[49] Cynthia Sung and Daniela Rus. Foldable Joints for Foldable Robots. *Journal of Mechanisms and Robotics*, 7(2), 05 2015. 021012.

[50] Landen Bowen, Kara Springsteen, Hannah Feldstein, Mary Frecker, Timothy W. Simpson, and Paris von Lockette. Development and Validation of a Dynamic Model of Magneto-Active Elastomer Actuation of the Origami Waterbomb Base. *Journal of Mechanisms and Robotics*, 7(1), 02 2015. 011010.

[51] Charles M. Wheeler and Martin L. Culpepper. Soft Origami: Classification, Constraint, and Actuation of Highly Compliant Origami Structures. *Journal of Mechanisms and Robotics*, 8(5), 05 2016. 051012.

[52] Hongbin Fang, K.W. Wang, and Suyi Li. Asymmetric energy barrier and mechanical diode effect from folding multi-stable stacked-origami. *Extreme Mechanics Letters*, 17:7 – 15, 2017.

[53] Qiuting Zhang, Jonathon Wommer, Connor O'Rourke, Joseph Teitelman, Yichao Tang, Joshua Robison, Gaojian Lin, and Jie Yin. Origami and kirigami inspired self-folding for programming three-dimensional shape shifting of polymer sheets with light. 2017.

[54] Bok Yeop Ahn, Daisuke Shoji, Christopher J. Hansen, Eunji Hong, David C. Dunand, and Jennifer A. Lewis. Printed origami structures. *Advanced Materials*, 22(20):2251–2254, 2010.

[55] J. Kimionis, M. Isakov, B. S. Koh, A. Georgiadis, and M. M. Tentzeris. 3d-printed origami packaging with inkjet-printed antennas for rf harvesting sensors. *IEEE Transactions on Microwave Theory and Techniques*, 63(12):4521–4532, Dec 2015.

[56] W. Su, S. A. Nauroze, B. Ryan, and M. M. Tentzeris. Novel 3d printed liquid-metal-alloy microfluidics-based zigzag and helical antennas for origami reconfigurable antenna "trees". In *2017 IEEE MTT-S International Microwave Symposium (IMS)*, pages 1579–1582, June 2017.

[57] Yiqi Mao, Kai Yu, Michael Isakov, Jiangtao Wu, Martin Dunn, and H. Qi. Sequential self-folding structures by 3d printed digital shape memory polymers. *Scientific reports*, 5:13616, 09 2015.

[58] T. Liu, Y. Wang, and K. Lee. Three-dimensional printable origami twisted tower: Design, fabrication, and robot embodiment. *IEEE Robotics and Automation Letters*, 3(1):116–123, Jan 2018.

[59] Yael Klein, Efi Efrati, and Eran Sharon. Shaping of elastic sheets by prescription of non-euclidean metrics. *Science*, 315(5815):1116–1120, 2007.

[60] Qi Ge, Conner K Dunn, H Jerry Qi, and Martin L Dunn. Active origami by 4d printing. *Smart Materials and Structures*, 23(9):094007, aug 2014.

[61] Tsz-Ho Kwok, Charlie C. L. Wang, Dongping Deng, Yunbo Zhang, and Yong Chen. Four-Dimensional Printing for Freeform Surfaces: Design Optimization of Origami and Kirigami Structures. *Journal of Mechanical Design*, 137(11), 10 2015. 111413.

[62] Xiaoming Mu, Nancy Sowan, Julia A Tumbic, Christopher N Bowman, Patrick T Mather, and Hang Jerry Qi. Photo-induced bending in a light-activated polymer laminated composite. *Soft matter*, 11 13:2673–82, 2015.

[63] Dongping Deng, Tsz-Ho Kwok, and Yong Chen. 4d printing: Design and fabrication of smooth curved surface using controlled self-folding. 2017.

[64] Qiuting Zhang, Jonathon Wommer, Connor O'Rourke, Joseph Teitelman, Yichao Tang, Joshua Robison, Gaojian Lin, and Jie Yin. Origami and kirigami inspired self-folding for programming three-dimensional shape shifting of polymer sheets with light. *Extreme Mechanics Letters*, 11:111 – 120, 2017.

[65] Niklas Kretzschmar, Sami Lipponen, Ville Klar, Joshua Pearce, Tom Ranger, Jukka Seppälä, and Jouni Partanen. Mechanical properties of ultraviolet-assisted paste extrusion and postextrusion ultraviolet-curing of three-dimensional printed biocomposites. *3D Printing and Additive Manufacturing*, 6, 05 2019.

[66] G.V. Salmoria, C.H. Ahrens, M. Fredel, V. Soldi, and A.T.N. Pires. Stereolithography somos 7110 resin: mechanical behavior and fractography of parts post-cured by different methods. *Polymer Testing*, 24(2):157 – 162, 2005.

[67] Xiao Kuang, Zeang Zhao, Kaijuan Chen, Daining Fang, Guozheng Kang, and Hang Jerry Qi. High-speed 3d printing of high-performance thermosetting polymers via two-stage curing. *Macromolecular Rapid Communications*, 39(7):1700809, 2018.

[68] Gerald Mitteramskogler, Robert Gmeiner, Ruth Felzmann, Simon Gruber, Christoph Hofstetter, Jürgen Stampfl, Jörg Ebert, Wolfgang Wachter, and Jürgen Laubersheimer. Light curing strategies for lithography-based additive manufacturing of customized ceramics. *Additive Manufacturing*, 1-4:110 – 118, 2014. Inaugural Issue.

[69] Ye Chan Kim, Sungyong Hong, Hanna Sun, Myeong Gi Kim, Kisuk Choi, Jungkeun Cho, Hyouk Ryeol Choi, Ja Choon Koo, Hyungpil Moon, Doyoung Byun, Kwang J. Kim, Jonghwan Suhr, Soo Hyun Kim, and Jae-Do Nam. Uv-curing kinetics and performance development of in situ curable 3d printing materials. *European Polymer Journal*, 93:140 – 147, 2017.

[70] Bernhard Steyrer, Philipp Neubauer, Robert Liska, and Jürgen Stampfl. Visible light photoinitiator for 3d-printing of tough methacrylate resins. *Materials*, 10(12), 2017.

[71] Dong Wu, Zeang Zhao, Qiang Zhang, H. Qi, and Daining Fang. Mechanics of shape distortion of dlp 3d printed structures during uv post – curing. *Soft Matter*, 06 2019.

[72] Leonid Ionov. Soft microorigami: self-folding polymer films. 2011.

[73] Leonid Ionov. Biomimetic 3d self-assembling biomicroconstructs by spontaneous deformation of thin polymer films. 2012.

[74] Mikell P. Groover. *Automation, Production Systems, and Computer-Integrated Manufacturing*. Pearson, USA, 4th edition, 2015.

[75] Jui-Teng Lin, Hsia-Wei Liu, Kuo-Ti Chen, and Da-Chuan Cheng. Modeling the kinetics, curing depth, and efficacy of radical-mediated photopolymerization: The role of oxygen inhibition, viscosity, and dynamic light intensity. *Frontiers in Chemistry*, 7:760, 2019.

[76] Jim H. Lee, Robert K. Prud'homme, and Ilhan A. Aksay. Cure depth in photopolymerization: Experiments and theory. *Journal of Materials Research*, 16(12):3536–3544, 2001.

[77] Aparna Boddapati. Modeling cure depth during photopolymerization of multifunctional acrylates. 05 2020.

[78] Jialu Wang and Xiaoyuan Liu. Generalized equations for estimating stress concentration factors of various notch flexure hinges. *Journal of Mechanical Design*, 136(3), 01 2014. 031009.

[79] J. M. Gere and Timoshenko. Mechanics of materials, 1997. pws publishing company.

[80] Landen Bowen, Kara Springsteen, Hannah Feldstein, Mary Frecker, Timothy W. Simpson, and Paris von Lockette. Development and Validation of a Dynamic Model of Magneto-Active Elastomer Actuation of the Origami Waterbomb Base. *Journal of Mechanisms and Robotics*, 7(1), 02 2015. 011010.

[81] W.D. Curtis, J.David Logan, and W.A. Parker. Dimensional analysis and the pi theorem. *Linear Algebra and its Applications*, 47:117 – 126, 1982.